ORIGINAL PAPER

Timon Rabczuk · Goangseup Zi

A meshfree method based on the local partition of unity for cohesive cracks

Abstract We will present a meshfree method based on the local partition of unity for cohesive cracks. The cracks are described by a jump in the displacement field for particles whose domain of influence is cut by the crack. Particles with partially cut domain of influence are enriched with branch functions. Crack propagation is governed by the material stability condition. Due to the smoothness and higher order continuity, the method is very accurate which is demonstrated for several quasi static and dynamic crack propagation examples.

Keywords Extended element-gree Galerkin method (XEFG) · Cracks · Cohesive models · Dynamic fracture

1 Introduction

Different methods have been presented to model cracks in finite element and meshfree methods. Simple and robust methods are interelement separation models in which cracks are modelled along element interfaces in the mesh, see Xu and Needleman [43], Camacho and Ortiz [17], Ortiz and Pandolfi [33], and Zhou and Molinari [44]. Another simple method was proposed by Remmers et al. [37] who introduced crack segments in finite elements. Rabczuk and Belytschko [34] developed a 'cracking particle' model in meshfree methods where discontinuities are introduced at the particle positions. The major advantage of these methods are their robustness and ease in implementation. However, for certain classes of problems, more accurate methods are needed.

The embedded discontinuity model [3, 7, 39] is another method for crack problems. However, its effectiveness in

T. Rabczuk (✉)
Institute for Numerical Mechanics, Technical University of Munich, Boltzmannstr. 15, 85748 Garching b. Munich, Germany
E-mail: Timon.Rabczuk@lnm.mw.tum.de
Tel.: +49-89-289915304

G. Zi
Department of Civil and Environmental Engineering, Korea University, 5-1, Anam-dong, Sungbuk- Ku, Seoul 136-701, Korea
E-mail: g-zi@korea.ac.kr

crack dynamics has still not been assessed and these methods require the crack to propagate one element at a time.

A very accurate method for crack problems is the extended finite element method (XFEM) developed by the group of Prof. Belytschko [5, 31]. This method is based on the 'local' partition of unity, in which the solution space is enriched by a priori knowledge about the behaviour of the solution near cracks. Because only the nodes belonging to the elements cut by cracks are enriched, the number of additional degrees of freedom for the local enrichment is minimized. The detailed discussion about the (local) partition of unity is found in the literature, e.g. Melenk and Babuska [30]; Chessa et al. [18]. This method has been successfully applied to static problems in two and three dimensions, (see e.g. [22, 31, 32, 45, 47]) and to dynamic problems ([6, 46]) in two dimensions.

Previous meshfree methods for cracking [9, 11, 14, 26, 29] in two and three dimensions were treated by the so called visibility criterion or some modifications of it. Therefore, the support is truncated by the line of discontinuity. Other novel approaches which were able to treat kinked and curve cracks were proposed by [41]. They also enriched the MLS base functions **p** around the crack tip and significantly improved the convergence behaviour. The major drawback is the need for an explicit representation of the crack.

A meshfree concept of XFEM was proposed by Ventura et al. [41] for linear elastic fracture mechanics in statics. We will pursue this idea and extend it to dynamics and cohesive cracks. The advantage of this meshfree method over XFEM is the higher smoothness, non-local interpolation character and higher order continuity which results in a better stress distribution around the crack tip which is important for the propagation of the crack.

In XFEM, mainly piecewise linear crack opening is assumed (due to the use of low order shape functions) but it is well known that in reality, the crack opening displacement is nonlinear, especially near the crack tip. Nonlinear crack opening relations can be easily incorporated in meshfree methods. In XFEM, Laborde et al. [27] have shown that a wider support for the crack tip enrichment improves the accuracy and convergence; more nodes are enriched for the
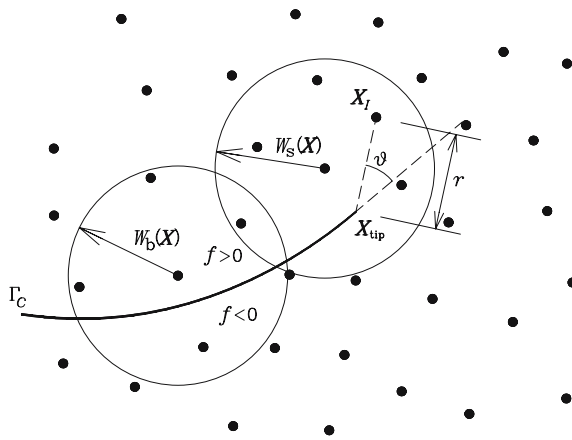
Fig. 1 Crack with partial cut and complete cut domain of influence particles

crack tip than in the classical XFEM. Meshfree methods naturally have a wider support due to their non-local interpolation character than FEM. However, this results in difficulties in imposing the Dirichlet boundary conditions at the crack, i.e. the crack has to close at the crack tip. A possible solution is addressed in the next section.

The paper is arranged as follows: in the next section, we will describe the concept, i.e. the approximation of the jump in the displacement. The meshfree method is briefly reviewed afterwards. In Sect. 4, we will give the governing equations and derive the discrete equations in Sect. 5. We will verify our model first for linear elastic fracture mechanics and compare results to former meshfree methods. Finally, we will solve several quasi-static and dynamic crack propagation problems and compare the results to experimental data or other data in the literature.

2 Approximation of the test and trial functions

The main idea to capture the crack is to enrich the test and trial functions with additional unknowns so that the approximation is continuous in the whole domain but discontinuous along the crack as done in many former methods such as XFEM [31]. Therefore, the test and trial functions are written in terms of a signed distance function f (see Fig. 1):

$$\delta \mathbf{u}(\mathbf{X}) = \sum_{I \in \mathcal{W}(\mathbf{X})} \Phi_I(\mathbf{X}) \, \delta \mathbf{u}_I$$
$$+ \sum_{I \in \mathcal{W}_b(\mathbf{X})} \Phi_I(\mathbf{X}) \, H\left(f_I(\mathbf{X})\right) \, \delta \mathbf{a}_I$$
$$+ \sum_{I \in \mathcal{W}_s(\mathbf{X})} \Phi_I(\mathbf{X}) \sum_K \mathbf{B}_K(\mathbf{X}) \, \delta \mathbf{b}_{KI} \qquad (1)$$
$$\mathbf{u}(\mathbf{X}) = \sum_{I \in \mathcal{W}(\mathbf{X})} \Phi_I(\mathbf{X}) \, \mathbf{u}_I$$
$$+ \sum_{I \in \mathcal{W}_b(\mathbf{X})} \Phi_I(\mathbf{X}) \, H\left(f_I(\mathbf{X})\right) \, \mathbf{a}_I$$

$$+ \sum_{I \in \mathcal{W}_s(\mathbf{X})} \Phi_I(\mathbf{X}) \sum_K \mathbf{B}_K(\mathbf{X}) \, \mathbf{b}_{KI} \qquad (2)$$

where $\mathcal{W}(\mathbf{X})$ is the entire domain, $\mathcal{W}_b(\mathbf{X})$ is the completely cut domain, $\mathcal{W}_s(\mathbf{X})$ is the partial cut domain, and H and $\mathbf{B}$ are the enrichment functions explained later. The first term on the right hand side of Eq. (1) or (2), respectively, is the usual approximation where Φ_I are the shape functions, and $\mathbf{u}_I$ and $\delta \mathbf{u}_I$ are the parameters. The second and third term is the enrichment, in which the coefficient $\delta \mathbf{a}$ and $\delta \mathbf{b}$ or $\mathbf{a}$ and $\mathbf{b}$, respectively, are additional unknowns introduced for the crack in the variational formulation.

$H(f(\mathbf{X}))$ depends on the signed distance function $f_I(\mathbf{X})$ and is defined as:

$$H\left(f_I(\mathbf{X})\right) = 1 \quad \text{if } f_I(\mathbf{X}) > 0$$
$$H\left(f_I(\mathbf{X})\right) = -1 \quad \text{if } f_I(\mathbf{X}) < 0 \qquad (3)$$

with

$$f_I(\mathbf{X})$$
$$= \begin{cases} \text{sign}[\mathbf{n} \cdot (\mathbf{X}_I - \mathbf{X})] \min \|\mathbf{X}_I - \mathbf{X}\|, & \text{for } \mathbf{X}_I \in \mathcal{W}_b \\ \mathbf{n} \cdot (\mathbf{X}_{\text{tip}} - \mathbf{X}_I), & \text{for } \mathbf{X}_I \in \mathcal{W}_s \end{cases}$$
$$(4)$$

where $\mathbf{X}_{\text{tip}}$ are the coordinates of the crack tip and $\mathbf{n}$ is the crack normal. Only nodes which are located in the domain $\mathcal{W}_b(\mathbf{X})$ are enriched with the additional unknowns $\delta \mathbf{a}$ and $\mathbf{a}$. The second term of Eq. (1) or (2) is called the 'step' enrichment.

The third term of Eqs. (1) and (2) is applied around the crack tip $\mathcal{W}_s(\mathbf{X})$. In linear elastic fracture mechanics, $\mathbf{B}$ is chosen to be continuous in the whole domain $\mathcal{W}_s(\mathbf{X})$, but discontinuous at the crack line:

$$\mathbf{B} = \left(\sqrt{r} \sin \frac{\theta}{2}, \sqrt{r} \cos \frac{\theta}{2}, \sqrt{r} \sin \frac{\theta}{2} \sin \theta, \right.$$
$$\left. \sqrt{r} \cos \frac{\theta}{2} \sin \theta \right) \qquad (5)$$

according to the analytical solution around the crack tip where r is the distance of $\mathbf{X}$ to the crack tip and $\theta(\mathbf{X}) = \sin^{-1}(f/r)$ is the angle between the tangent to the crack line and the segment $\mathbf{X} - \mathbf{X}_{\text{tip}}$, see Fig. 1. It is called the 'branch' enrichment.

For cohesive cracks, there is no crack tip singularity and the crack opening displacement, which the cohesive traction depends on, may be described by the additional unknown $\mathbf{a}$ only. In XFEM, this procedure is straightforward since it is easy to impose the appropriate boundary conditions, see Fig. 2a, i.e. the crack has to close at the end of the element edge. This can be accomplished e.g. by not enriching the nodes at the element edge where the crack tip is located as shown in Fig. 2a. However, in meshfree methods, this technique cannot be applied analogous to the way in XFEM, see Fig. 2b.

Therefore, we keep the branch enrichment for cohesive cracks, but without the crack tip singularity:

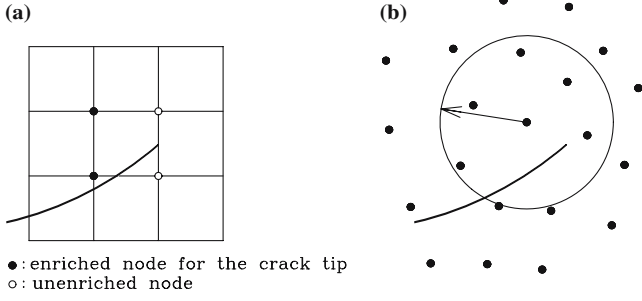$$\mathbf{B} = \left(r^m \sin \frac{\theta}{2} \right) \quad m = 1, 2, 3 \qquad (6)$$

Fig. 2 Crack with enriched nodes in **a** XFEM and **b** meshfree methods

Fig. 3 Support of node I with **a** intersecting discontinuities and **b** branching discontinuities

While lower order finite elements (that are usually applied) can capture only linear crack opening, meshfree methods have the advantage to capture more realistic crack openings, as measured in experiments, due to their ease of increasing the order of continuity. Another advantage is the non-local interpolation character, i.e. many particles are enriched. We have tested the branch functions, Eq. (6), for cohesive cracks.

Furthermore, we shifted the function $H_I(f(\mathbf{X}))$ and $\mathbf{B}_K(\mathbf{X})$ by their values at the position of particle I, i.e. $H_I(f(\mathbf{X}_I))$ and $\mathbf{B}_K(\mathbf{X}_I)$, respectively:

$$\bar{H}_I^n(\mathbf{X}) = H^n\left(f^n(\mathbf{X})\right) - H^n\left(f^n(\mathbf{X}_I)\right) \qquad (7)$$

$$\bar{\mathbf{B}}_K^m(\mathbf{X}) = \mathbf{B}_K^m(\mathbf{X}) - \mathbf{B}_K^m(\mathbf{X}_I) \qquad (8)$$

which makes the enriched region narrower. To avoid having heavy notations, we drop ¯ in the following sections; unless mentioned otherwise, H and $\mathbf{B}$ stand for $\bar{H}$ and $\bar{\mathbf{B}}$ of Eqs. (7) and (8), respectively.

We would like to mention that for particles in the blending region, i.e. the particles whose domain of influence is not cut but influenced by the 'enriched' particles, only the 'usual' approximation [first term on the right hand side of Eqs. (1) and (2)] is considered in the approximation of the test and trial functions.

2.1 Tracing the crack paths

The level set techniques is often used to trace the crack paths, Moes et al. [31]; Ventura et al. [41]; Belytschko et al. [12]; Rabczuk and Belytschko [35]. We believe it is easier to trace the crack paths by piecewise linear lines. However, in certain cases, e.g. for non-linear crack paths, the use of level sets can be advantageous. The crack is defined by an implicit function f which is zero along the crack path and has the value of the minimum distance to the crack with plus or minus sign. The choice of the sign is completely arbitrary as long as it is consistent throughout the entire calculation. We will not explain the crack tracing procedure with level sets in more detail and refer the interested reader to the literature, e.g. [12, 31, 41]. However, we briefly describe how to treat crack branching and crack intersection which is different from the approach in [19] and [12] in the sense that we do not use any special branch function in addition to the 'usual' enrichment. Consider cracks shown in Fig. 3. Let $\mathcal{W}_b^1$ be the set of
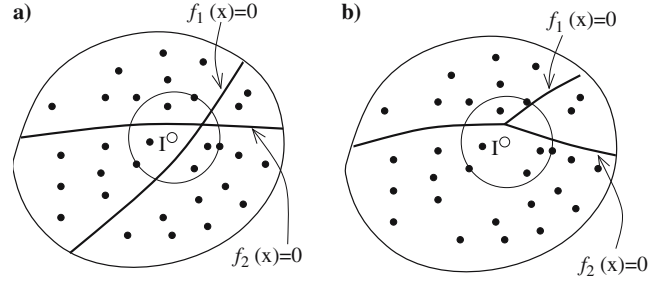
nodes whose domain of influence is completely cut by the discontinuity $f_1(\mathbf{X}) = 0$ and $\mathcal{W}_b^2$ the corresponding set for $f_2(\mathbf{X}) = 0$. $\mathcal{W}_b^3 = \mathcal{W}_b^1 \bigcap \mathcal{W}_b^2$. The same applies accordingly for nodes whose domain of influence is cut by the crack tip enrichment. We will denote this set of nodes with $\mathcal{W}_s^1$ and $\mathcal{W}_s^2$. Then the approximation of the displacement may be given by [19]

$$\begin{aligned}
\mathbf{u}(\mathbf{X}) = &\sum_{I \in \mathcal{W}(\mathbf{X})} \Phi_I(\mathbf{X})\, \mathbf{u}_I \\
&+ \sum_{I \in \mathcal{W}_b^1(\mathbf{X})} \Phi_I(\mathbf{X})\, H(f_1(\mathbf{X}))\, \mathbf{a}_I^{(1)} \\
&+ \sum_{I \in \mathcal{W}_b^2(\mathbf{X})} \Phi_I(\mathbf{X})\, H(f_2(\mathbf{X}))\, \mathbf{a}_I^{(2)} \\
&+ \sum_{I \in \mathcal{W}_b^3(\mathbf{X})} \Phi_I(\mathbf{X})\, H(f_1(\mathbf{X}))\, H(f_2(\mathbf{X}))\, \mathbf{a}_I^{(3)} \\
&+ \sum_{I \in \mathcal{W}_s^1(\mathbf{X})} \Phi_I(\mathbf{X}) \sum_K \mathbf{B}_K^{(1)}(\mathbf{X})\, \mathbf{b}_{KI}^{(1)} \\
&+ \sum_{I \in \mathcal{W}_s^2(\mathbf{X})} \Phi_I(\mathbf{X}) \sum_K \mathbf{B}_K^{(2)}(\mathbf{X})\, \mathbf{b}_{KI}^{(2)} \qquad (9)
\end{aligned}$$

Principally, more than two branches can be included at one time and a branched crack can branch again. As can be easily seen by Eq. (9), additional complexity is then introduced. We would like to mention, that Eq. (9) looks worse than it is since only very few nodes are included in all sets $\mathcal{W}$. However, a crack branching requires the introduction of another level set which makes the computation cumbersome for many cracks.

Zi et al. [47] proposed a computationally more efficient approach than (9) by modifying the signed distance functions so that no cross terms are needed for junction or branch problems.

When two cracks are joining, the crack tip enrichment is removed. By using the signed distance functions of the pre-existing and approaching crack, the signed distance function of the approaching crack is modified. Consider Fig. 4. Three different subdomains have to be considered: $(f_1 < 0, f_2 < 0)$, $(f_1 > 0, f_2 > 0)$, $(f_1 > 0, f_2 < 0)$ as in Fig. 4b or $(f_1 > 0, f_2 < 0)$, $(f_1 > 0, f_2 > 0)$, $(f_1 < 0, f_2 < 0)$ as in Fig. 4d. The signed distance function of crack 1 of a point $\mathbf{X}$
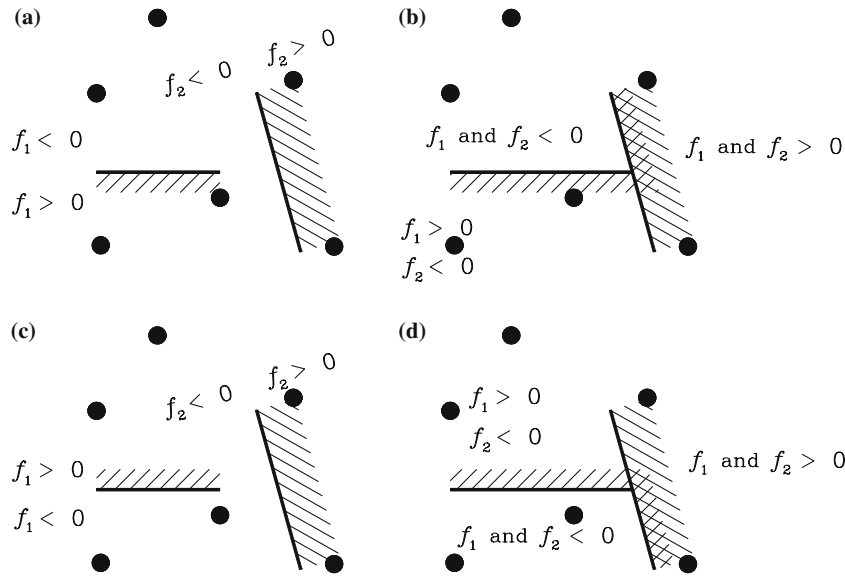
Fig. 4 Sign functions for crack junction

is then obtained by:

$$f_1(\mathbf{X}) = \begin{cases} f_1^0(\mathbf{X}), & \text{if } f_2^0(\mathbf{X_1})\, f_2^0(\mathbf{X}) > 0 \\ f_2^0(\mathbf{X}), & \text{if } f_2^0(\mathbf{X_1})\, f_2^0(\mathbf{X}) < 0 \end{cases} \tag{10}$$

where the superimposed 0 denotes the sign distance function before crack junction. Therefore, the final approximation without the cross term reads:

$$\begin{aligned} \mathbf{u}(\mathbf{X}) = &\sum_{I \in \mathcal{W}(\mathbf{X})} \Phi_I(\mathbf{X})\, \mathbf{u}_I \\ &+ \sum_{n=1}^{n_c} \sum_{I \in \mathcal{W}_b(\mathbf{X})} \Phi_I(\mathbf{X})\, H\left(f_I^{(n)}(\mathbf{X})\right) \mathbf{a}_I^{(n)} \\ &+ \sum_{m=1}^{m_t} \sum_{I \in \mathcal{W}_s(\mathbf{X})} \Phi_I(\mathbf{X}) \sum_K \mathbf{B}_K^{(m)}(\mathbf{X})\, \mathbf{b}_{KI}^{(m)} \end{aligned} \tag{11}$$

where n_c and m_t are the number of cracks that completely or partially, respectively, cross the domain of influence of the corresponding particle. The test functions are expressed according to Eq. (11):

$$\begin{aligned} \delta\mathbf{u}(\mathbf{X}) = &\sum_{I \in \mathcal{W}(\mathbf{X})} \Phi_I(\mathbf{X})\, \delta\mathbf{u}_I \\ &+ \sum_{n=1}^{n_c} \sum_{I \in \mathcal{W}_b(\mathbf{X})} \Phi_I(\mathbf{X})\, H\left(f_I^{(n)}(\mathbf{X})\right) \delta\,\mathbf{a}_I^{(n)} \\ &+ \sum_{m=1}^{m_t} \sum_{I \in \mathcal{W}_s(\mathbf{X})} \Phi_I(\mathbf{X}) \sum_K \mathbf{B}_K^{(m)}(\mathbf{X})\, \delta\mathbf{b}_{KI}^{(m)} \end{aligned} \tag{12}$$

3 Meshfree approximation

The meshfree approximation can be written as

$$\mathbf{u}(\mathbf{X}, t) = \sum_I \Phi_I(\mathbf{X})\, \mathbf{u}_I(t) \tag{13}$$

In the EFG-method (see e.g. [8–10]), the shape functions are calculated as follows:

$$\Phi_J = \mathbf{p}(\mathbf{X})^{\mathrm{T}}\, \mathbf{A}(\mathbf{X})^{-1}\, \mathbf{D}(\mathbf{X}_J) \tag{14}$$

$$\mathbf{A}(\mathbf{X}) = \sum_J \mathbf{p}(\mathbf{X}_J)\, \mathbf{p}^{\mathrm{T}}(\mathbf{X}_J)\, W(\mathbf{X} - \mathbf{X}_J, h) \tag{15}$$

$$\mathbf{D}(\mathbf{X}_J) = \mathbf{p}(\mathbf{X}_J)\, W(\mathbf{X} - \mathbf{X}_J, h) \tag{16}$$

Hereby, $\mathbf{p}$ are the base polynomials, W is the kernel function, and h is the size of the domain of influence. To ensure the conservation of angular momentum, the approximation has to be linear complete. Therefore, the base polynomials are chosen to be $\mathbf{p} = (1, X, Y)$.

In addition to the fact that the order of continuity can be increased quite easily, meshfree methods have advantages over finite elements because of their smoothness and nonlocal interpolation character. Better stress distributions around the crack tip are expected, which must lead to a less-oscillatory crack propagation.

Continuity in meshfree methods is governed by the continuity of the kernel function W. We used the cubic B-Spline as the kernel that is C^2.

4 Governing equations

The strong form of the momentum equation in a total Lagrangian description is given by

$$\varrho_0\, \ddot{\mathbf{u}} = \nabla_0 \cdot \mathbf{P} + \varrho_0\, \mathbf{b} \quad \text{in } \Omega_0 \setminus \Gamma_0^c \tag{17}$$

with boundary conditions:

$$\mathbf{u}(\mathbf{X}, t) = \bar{\mathbf{u}}(\mathbf{X}, t) \quad \text{on} \quad \Gamma_0^u \tag{18}$$

$$\mathbf{n}_0 \cdot \mathbf{P}(\mathbf{X}, t) = \bar{\mathbf{t}}_0(\mathbf{X}, t) \quad \text{on} \quad \Gamma_0^t \tag{19}$$

$$\mathbf{n}_0 \cdot \mathbf{P}^- = \mathbf{n}_0 \cdot \mathbf{P}^+ = \mathbf{t}_{c0} \text{ on } \Gamma_0^c \tag{20}$$

$$\mathbf{t}_{c0} = \mathbf{t}_{c0}(\llbracket \mathbf{u} \rrbracket) \text{ on } \Gamma_0^c \tag{21}$$

where ϱ_0 is the initial density, $\ddot{\mathbf{u}}$ is the acceleration, $\mathbf{P}$ denotes the nominal stress tensor, $\mathbf{b}$ designates the body force, $\bar{\mathbf{u}}$ and $\bar{\mathbf{t}}_0$ are the prescribed displacement and traction, respectively, $\mathbf{n}_0$ is the outward normal to the domain and $\Gamma_0^u \bigcup \Gamma_0^t \bigcup \Gamma_0^c = \Gamma_0$, $(\Gamma_0^u \bigcap \Gamma_0^t) \bigcup (\Gamma_0^t \bigcap \Gamma_0^c) \bigcup (\Gamma_0^c \bigcap \Gamma_0^u) = \emptyset$. Moreover, we assume that the stresses $\mathbf{P}$ at the crack surface Γ_0^c are bounded. Since the stresses are not well defined in the crack, the crack surface Γ_0^c is excluded from the domain Ω_0 which is considered as an open set.

5 The discrete momentum equation

Starting point is the weak form of the momentum equation which is given by

$$\delta W = \delta W_{\text{int}} - \delta W_{\text{ext}} + \delta W_{\text{kin}} = 0 \tag{22}$$

where

$$\delta W_{\text{int}} = \int_{\Omega_0 \setminus \Gamma_0^c} (\nabla \otimes \delta \mathbf{u})^{\mathrm{T}} : \mathbf{P} \, d\Omega_0 \tag{23}$$

$$\delta W_{\text{ext}} = \int_{\Omega_0 \setminus \Gamma_0^c} \varrho_0 \, \delta \mathbf{u} \cdot \mathbf{b} \, d\Omega_0 + \int_{\Gamma_0^t} \delta \mathbf{u} \cdot \bar{\mathbf{t}}_0 \, d\Gamma_0$$

$$+ \int_{\Gamma_0^c} [\![\delta \mathbf{u}]\!] \cdot \mathbf{t}_c 0 \, d\Gamma_0 \tag{24}$$

$$\delta W_{\text{kin}} = \int_{\Omega_0 \setminus \Gamma_0^c} \varrho_0 \, \delta \mathbf{u} \cdot \ddot{\mathbf{u}} \, d\Omega_0 \tag{25}$$

Substituting the test and trial functions (Eqs. (11) and (12), respectively) into Eqs. (23) to (25), we obtain

$$W_{\text{kin}} = \int_{\Omega_0 \setminus \Gamma_0^c} \varrho_0 \, \left(\Phi_I(\mathbf{X}) \, \delta \mathbf{u}_I \right.$$

$$+ \Phi_I(\mathbf{X}) \, H\left(f_I^{(n)}(\mathbf{X})\right) \, \delta \mathbf{a}_I^{(n)}$$

$$+ \Phi_I(\mathbf{X}) \, \mathbf{B}_K^{(m)} \, \delta \mathbf{b}_{KI}^{(m)} \bigg)$$

$$\cdot \left(\Phi_J(\mathbf{X}) \, \ddot{\mathbf{u}}_J \right.$$

$$+ \Phi_J(\mathbf{X}) H\left(f_J^{(n)}(\mathbf{X})\right) \, \ddot{\mathbf{a}}_J^{(n)}$$

$$+ \Phi_J(\mathbf{X}) \, \mathbf{B}_K^{(m)} \, \ddot{\mathbf{b}}_{KJ}^{(m)} \bigg) \, d\Omega_0 \tag{26}$$

$$W_{\text{int}} = \int_{\Omega_0 \setminus \Gamma_0^c} \delta \mathbf{u}_I \, \nabla_0 \Phi_I(\mathbf{X}) \cdot \mathbf{P} \, d\Omega_0$$

$$+ \int_{\Omega_0 \setminus \Gamma_0^c} \delta \mathbf{a}_I^{(n)} \left[\nabla_0 \Phi_I(\mathbf{X}) \, H\left(f_I^{(n)}(\mathbf{X})\right) \right.$$

$$+ \Phi_I(\mathbf{X}) \nabla_0 H\left(f_I^{(n)}(\mathbf{X})\right) \bigg] \cdot \mathbf{P} \, d\Omega_0$$

$$+ \int_{\Omega_0 \setminus \Gamma_0^c} \left[\left(\nabla_0 \Phi_I(\mathbf{X}) \, \mathbf{B}_K^{(m)} \right. \right.$$

$$+ \Phi_I(\mathbf{X}) \, \nabla_0 \mathbf{B}_K^{(m)} \bigg) \delta \mathbf{b}_{KI}^{(m)} \bigg] \cdot \mathbf{P} \, d\Omega_0 \tag{27}$$

$$\int_{\Omega_0 \setminus \Gamma_0^c} \varrho_0 \, \delta \mathbf{u} \cdot \mathbf{b} \, d\Omega_0 = \int_{\Omega_0 \setminus \Gamma_0^c} \varrho_0 \, \left(\Phi_I(\mathbf{X}) \, \delta \mathbf{u}_I \right.$$

$$+ \Phi_I(\mathbf{X}) \, H\left(f_I^{(n)}(\mathbf{X})\right) \, \delta \mathbf{a}_I^{(n)}$$

$$+ \Phi_I(\mathbf{X}) \, \mathbf{B}_K^{(m)} \, \delta \mathbf{b}_I^{(m)} \bigg) \cdot \mathbf{b} \, d\Omega_0 \tag{28}$$

$$\int_{\Gamma_0^t} \delta \mathbf{u} \cdot \bar{\mathbf{t}}_0 \, d\Gamma_0 = \int_{\Gamma_0^t} \left(\Phi_I(\mathbf{X}) \delta \mathbf{u}_I + \Phi_I(\mathbf{X}) H\left(f_I^{(n)}(\mathbf{X})\right) \delta \mathbf{a}_I^{(n)} \right.$$

$$+ \Phi_I(\mathbf{X}) \mathbf{B}_K^{(m)} \, \delta \mathbf{b}_{KI}^{(m)} \bigg) \cdot \bar{\mathbf{t}}_0 \, d\Gamma_0 \tag{29}$$

$$\int_{\Gamma_0^c} [\![\delta \mathbf{u}]\!] \cdot \mathbf{t}_c 0 \, d\Gamma_0 = \int_{\Gamma_0^c} \bigg[\!\bigg[\Phi_I(\mathbf{X}) \delta \mathbf{u}_I + \Phi_I(\mathbf{X}) H\left(f_I^{(n)}(\mathbf{X})\right) \delta \mathbf{a}_I^{(n)}$$

$$+ \Phi_I(\mathbf{X}) \, \mathbf{B}_K^{(m)} \, \delta \mathbf{b}_{KI}^{(m)} \bigg]\!\bigg] \cdot \mathbf{t}_c 0 \, d\Gamma_0$$

$$= \int_{\Gamma_0^c} \bigg[\!\bigg[\Phi_I(\mathbf{X}) \, H\left(f_I^{(n)}(\mathbf{X})\right) \, \delta \mathbf{a}_I^{(n)}$$

$$+ \Phi_I(\mathbf{X}) \, \mathbf{B}_K^{(m)} \, \delta \mathbf{b}_{KI}^{(m)} \bigg]\!\bigg] \cdot \mathbf{t}_c 0 \, d\Gamma_0 \tag{30}$$

where Eqs. (28) to (30) are for W_{ext}. After some algebraic operations the final form of the equation of motion is obtained by

$$\mathbf{M}_{IJ} \cdot \ddot{\mathbf{u}}_I = \mathbf{F}_I^{\text{ext}} - \mathbf{F}_I^{\text{int}} \tag{31}$$

with

$$\mathbf{M}_{IJ} = \begin{bmatrix} \mathbf{m}_{IJ}^{uu} & \mathbf{m}_{IJ}^{ua} & \mathbf{m}_{IJ}^{ub} \\ \mathbf{m}_{IJ}^{au} & \mathbf{m}_{IJ}^{aa} & \mathbf{m}_{IJ}^{ab} \\ \mathbf{m}_{IJ}^{bu} & \mathbf{m}_{IJ}^{ba} & \mathbf{m}_{IJ}^{bb} \end{bmatrix} \tag{32}$$

$$\ddot{\mathbf{u}}_I = \begin{bmatrix} \ddot{\mathbf{u}}_I^u \\ \ddot{\mathbf{a}}_I \\ \ddot{\mathbf{b}}_{IK} \end{bmatrix} \tag{33}$$

$$\mathbf{F}_I^{\text{ext}} = \begin{bmatrix} \mathbf{f}_I^{u,\text{ext}} \\ \mathbf{f}_I^{a,\text{ext}} \\ \mathbf{f}_{IK}^{b,\text{ext}} \end{bmatrix} \tag{34}$$

$$\mathbf{F}_I^{\text{int}} = \begin{bmatrix} \mathbf{f}_I^{u,\text{int}} \\ \mathbf{f}_I^{a,\text{int}} \\ \mathbf{f}_{IK}^{b,\text{int}} \end{bmatrix} \tag{35}$$

with

$$\mathbf{m}_{IJ}^{uu} = \int_{\Omega_0 \setminus \Gamma_0^c} \varrho_0 \, \Phi_I(\mathbf{X}) \, \Phi_J(\mathbf{X}) \, d\Omega_0$$

$$\mathbf{m}_{IJ}^{ua} = \int_{\Omega_0 \setminus \Gamma_0^c} \varrho_0 \, \Phi_I(\mathbf{X}) \, \Phi_J(\mathbf{X}) \, H\left(f_I^{(n)}(\mathbf{X})\right) \, d\Omega_0 \,,$$

$$\mathbf{m}_{IJ}^{ua} = \mathbf{m}_{IJ}^{au}$$

$$\mathbf{m}_{IJ}^{ub} = \int_{\Omega_0 \setminus \Gamma_0^c} \varrho_0 \, \Phi_I(\mathbf{X}) \, \Phi_J(\mathbf{X}) \, \mathbf{B}_K^{(m)} \, d\Omega_0 \,,$$

$$\mathbf{m}_{IJ}^{ub} = \mathbf{m}_{IJ}^{bu}$$

$$\mathbf{m}_{IJ}^{aa} = \int_{\Omega_0 \backslash \Gamma_0^c} \varrho_0 \, \Phi_I(\mathbf{X}) \, H\left(f_I^{(n)}(\mathbf{X})\right)$$

$$\varphi_J(\mathbf{X}) \, H\left(f_I^{(n)}(\mathbf{X})\right) \, d\Omega_0$$

$$\mathbf{m}_{IJ}^{ab} = \int_{\Omega_0 \backslash \Gamma_0^c} \varrho_0 \, \Phi_I(\mathbf{X}) \, H\left(f_I^{(n)}(\mathbf{X})\right)$$

$$\varphi_J(\mathbf{X}) \, \mathbf{B}_K^{(m)} \, d\Omega_0, \quad \mathbf{m}_{IJ}^{ab} = \mathbf{m}_{IJ}^{ba}$$

$$\mathbf{m}_{IJ}^{bb} = \int_{\Omega_0 \backslash \Gamma_0^c} \varrho_0 \, \Phi_I(\mathbf{X}) \, \mathbf{B}_K^{(m)} \, \Phi_J(\mathbf{X}) \, \mathbf{B}_K^{(m)} \, d\Omega_0 \qquad (36)$$

$$\mathbf{f}_I^{u,\text{ext}} = \int_{\Omega_0 \backslash \Gamma_0^c} \varrho_0 \, \mathbf{b} \, \Phi_I(\mathbf{X}) \, d\Omega_0$$

$$+ \int_{\Gamma_0^t} \bar{\mathbf{t}}_0 \, \Phi_I(\mathbf{X}) \, d\Gamma_0 + \mathbf{f}_I^{u,cr}$$

$$\mathbf{f}_I^{a,\text{ext}} = \int_{\Omega_0 \backslash \Gamma_0^c} \varrho_0 \, \mathbf{b} \, \Phi_I(\mathbf{X}) \, H\left(f_I^{(n)}(\mathbf{X})\right) \, d\Omega_0$$

$$+ \int_{\Gamma_0^t} \bar{\mathbf{t}}_0 \, \Phi_I(\mathbf{X}) \, H\left(f_I^{(n)}(\mathbf{X})\right) \, d\Gamma_0 + \mathbf{f}_I^{a,cr}$$

$$\mathbf{f}_I^{b,\text{ext}} = \int_{\Omega_0 \backslash \Gamma_0^c} \varrho_0 \, \mathbf{b} \, \Phi_I(\mathbf{X}) \, \mathbf{B}_K^{(m)} \, d\Omega_0$$

$$+ \int_{\Gamma_0^t} \bar{\mathbf{t}}_0 \, \Phi_I(\mathbf{X}) \, \mathbf{B}_K^{(m)} \, d\Gamma_0 + \mathbf{f}_I^{b,cr} \qquad (37)$$

where

$$\mathbf{f}_I^{a,\text{cr}} = \int_{\Gamma_0^c} \Phi_I(\mathbf{X}) \left[\!\left[H\left(f_I^{(n)}(\mathbf{X})\right) \right]\!\right] \mathbf{t}_c 0 \, d\Gamma_0$$

$$\mathbf{f}_I^{b,\text{cr}} = \int_{\Gamma_0^c} \Phi_I(\mathbf{X}) \left[\!\left[\mathbf{B}_K^{(m)} \right]\!\right] \mathbf{t}_c 0 \, d\Gamma_0 \qquad (38)$$

$$\mathbf{f}_I^{u,\text{int}} = \int_{\Omega_0 \backslash \Gamma_0^c} \nabla_0 \Phi_I(\mathbf{X}) \cdot \mathbf{P} \, d\Omega_0$$

$$\mathbf{f}_I^{a,\text{int}} = \int_{\Omega_0 \backslash \Gamma_0^c} \left(\left(\nabla_0 \Phi_I(\mathbf{X}) \, H\left(f_I^{(n)}(\mathbf{X})\right) \right. \right.$$

$$\left. \left. + \, \Phi_I(\mathbf{X}) \, \nabla_0 H\left(f_I^{(n)}(\mathbf{X})\right) \right) \cdot \mathbf{P} \right) d\Omega_0$$

$$\mathbf{f}_{IK}^{b,\text{int}} = \int_{\Omega_0 \backslash \Gamma_0^c} \left(\left(\nabla_0 \Phi_I(\mathbf{X}) \, \mathbf{B}_K^{(m)} \right. \right.$$

$$\left. \left. + \, \Phi_I(\mathbf{X}) \, \nabla_0 \mathbf{B}_K^{(m)} \right) \cdot \mathbf{P} \right) d\Omega_0 \qquad (39)$$

Equation (36) is the consistent mass matrix. In Eq. (39), the spatial derivatives of H vanish since the domain is considered as an open set. The cohesive forces are taken into
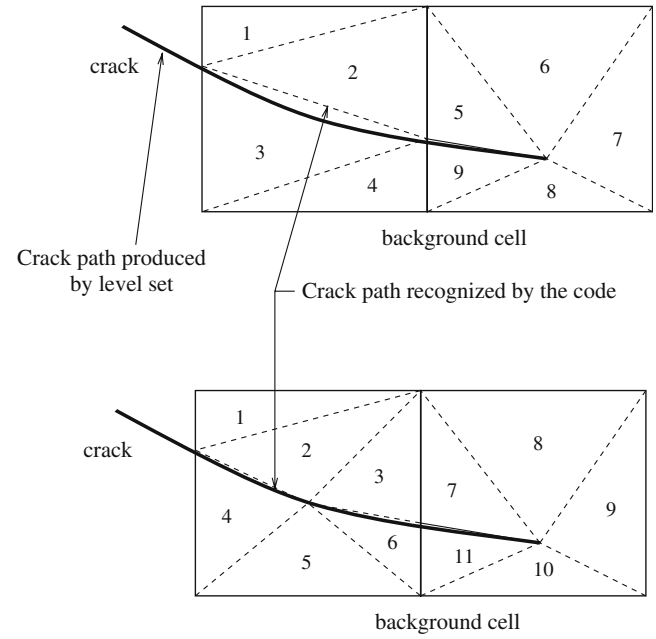

Fig. 5 Sub-triangulation of background cells

account in the external forces, Eq. (37). Gauss quadrature is used to obtain the discrete equations. Generally, four nodes are arranged so that they form the quadrature cell. Integration cells cut by a crack are sub-triangulated as in XFEM. Note, that the crack tip does not necessarily cross the entire background cell, see Fig. 5 for possible sub-triangulations. Quadrature points are added to the new sampling points. The integration may be erroneous if any sampling points for triangle 3 is positioned above of the actual crack path, see Fig. 5. To minimize such an error, a point in the middle of the crack path in the cell is added as shown in the bottom Fig. 5. Adding one more point, the error is reduced second order small.

In LEFM, care should be taken at the crack tip since a singularity is present. Laborder et al. [27] found an elegant solution by expressing the integral in polar coordinates that gave excellent results even for very small number of integration points. This may be implemented in the method presented. Since we were mainly interested in nonlinear materials without the crack tip singularity, we did not do any special arrangements near the crack tip.

An alternative of this approach that does not require triangulation of the background cell would be the appropriate modification of the integration weights. For more details, see Areias et al. [2].

The cohesive tractions across the crack are integrated by the standard surface integration.

6 Constitutive model

6.1 Continuum model

We used Rankine type materials, the Lemaitre damage model [28] and the Johnson–Cook model [24]. For the Lemaitre

model, the stress–strain behaviour is given by

$$\boldsymbol{\sigma} = (1 - D) \, \mathbf{C} : \boldsymbol{\epsilon} \tag{40}$$

where D is a scalar damage variable which ranges from 0 to a maximum of 1 and $\mathbf{C}$ is the initial elasticity tensor. The damage evolution depends on the effective strain $\bar{\epsilon}$:

$$D(\bar{\epsilon}) = 1 - (1 - A) \, \epsilon_{D_0} \, \bar{\epsilon}^{-1} - A \mathrm{e}^{-B(\bar{\epsilon} - \epsilon_{D_0})} \tag{41}$$

with

$$\bar{\epsilon} = \sqrt{\sum_{i=1}^{3} \epsilon_i^2 \, \mathcal{H}(\epsilon_i)} \tag{42}$$

where ϵ_i are the principal strains and with

$$\mathcal{H}(x) = 1 \quad \text{if } x > 0$$
$$\mathcal{H}(x) = 0 \quad \text{if } x < 0 \tag{43}$$

A, B and ϵ_{D_0} are material parameters.

The Johnson–Cook model [24] is based on J_2 plasticity but takes into account strain rate and temperature effects. The effective yield stress of the Johnson–Cook model is given by

$$\sigma_{\mathrm{Y}} = \left(A + B\gamma^n\right) \left(1 + C \ln \dot{\epsilon}^*\right) \left(1 - T^*\right) \tag{44}$$

where $\dot{\epsilon}^* = \dot{\gamma}/\dot{\gamma}_0$, γ is the effective plastic strain, $\dot{\gamma}_0$ is the reference strain rate taken to be 1.0/s and A, B, C are material parameters, respectively. T^* is given by

$$T^* = \frac{T - T_{\mathrm{r}}}{T_{\mathrm{m}} - T_{\mathrm{r}}} \tag{45}$$

where T_{r} is the reference temperature and T_{m} is the melting temperature. We assume that the plastic deformation is completely transformed into heat, so $\beta = 1$ for the temperature update:

$$\Delta T = \int_0^{\gamma} \frac{\beta}{\varrho c_v} \sigma_{\mathrm{Y}} d\gamma \tag{46}$$

where ϱ is the mass density and c_v is the specific heat per unit mass.

Gummalle [23] pointed out that the initial negative slope of the effective plastic stress–effective plastic strain curve highly determines the shear band initiation. He suggested the following form of the effective yield stress that gave better results in his computations:

$$\sigma_{\mathrm{Y}} = \max \left[\left(A + B\gamma^n\right) \left(1 + C \ln \dot{\epsilon}^*\right) \right.$$
$$\left. \left(1 - \delta \left(\exp\left(\frac{T - T_0}{\kappa_0}\right) - 1\right)\right), 0\right] \tag{47}$$

6.2 Cohesive crack model

6.2.1 Cracking criteria

We employed the loss of hyperbolicity criterion for crack initiation and propagation. Therefore, a crack is initiated or propagated if the minimum eigenvalue of the acoustic tensor $\mathbf{Q}$ is smaller or equal to zero:

$$\min \mathrm{eig}(\mathbf{Q}) \leq 0 \quad \text{with } \mathbf{Q} = \mathbf{n} \cdot \mathbf{A} \cdot \mathbf{n} \quad \text{and} \quad \mathbf{A} = \mathbf{C}^{\mathrm{t}} + \boldsymbol{\sigma} \otimes \mathbf{I} \tag{48}$$

where $\mathbf{n} = [\cos(\theta) \quad \sin(\theta)]$ is the normal to the crack surface depending on the angle θ, $\mathbf{C}^{\mathrm{t}}$ is the fourth order tangential modulus tensor and $\mathbf{I}$ is the second order identity tensor.

For a crack propagation, we checked the loss of hyperbolicity condition in a half circle around the crack tip for every material point. If the PDE looses hyperbolicity at one material point, the crack is advanced from the crack tip. The direction of crack propagation is completely determined by $\mathbf{n}$ obtained from the localization analysis. Crack branching occurs if the PDE looses hyperbolicity at two material points with different $\mathbf{n}$. Now, it still remains the question of how to propagate the crack.

There are numerous possibilities how to determine the crack velocity. The easiest way is to control the crack length, [45]. However, we believe this approach is not accurate enough and adopt an approximation suggested by Belytschko et al. [6]. Key assumption is that the hyperbolicity indicator $e = \mathbf{h} \cdot \mathbf{Q} \cdot \mathbf{h}$ must vanish at the crack tip:

$$\frac{\partial e}{\partial t} + \mathbf{v}^{\mathrm{c}} \cdot \nabla e = 0 \quad \text{with} \quad \mathbf{v}^{\mathrm{c}} = v^{\mathrm{c}} \, \mathbf{s} \tag{49}$$

where v^{c} is the crack speed, $\mathbf{s}$ gives its direction which must fulfill the condition $\mathbf{n} \cdot \mathbf{s} = 0$ and $\mathbf{h}$ is assumed to be parallel to $\mathbf{n}$ ($\mathbf{h}$ is the eigenvector of $\mathbf{Q}$ obtained from the localization analysis). To obtain the crack length, the Eq. (49) has to be solved for v^{c}. In [6], they used an incremental version of $\mathbf{s}$ though the advantage is not clear to us. Hence, we used the rate form of the hyperbolicity indicator.

6.2.2 Jump in the displacement

The jump in the displacement is governed only by the enrichment and is given by

$$[\![\mathbf{u}(\mathbf{X})]\!] = \sum_{n=1}^{n_c} \sum_{I \in \mathcal{W}_b(\mathbf{X})} \Phi_I(\mathbf{X}) [\![H(\mathbf{X})]\!] \mathbf{q}_I$$
$$+ \sum_{m=1}^{m_t} \sum_{I \in \mathcal{W}_s(\mathbf{X})} \Phi_I(\mathbf{X}) \sum_K [\![\mathbf{B}_K(\mathbf{X})]\!] \mathbf{b}_{KI}$$
$$= 2 \sum_{n=1}^{n_c} \sum_{I \in \mathcal{W}_b(\mathbf{X})} \Phi_I(\mathbf{X}) \mathbf{q}_I$$
$$+ \sum_{m=1}^{m_t} \sum_{I \in \mathcal{W}_s(\mathbf{X})} \Phi_I(\mathbf{X}) \sum_K [\![\mathbf{B}_K(\mathbf{X})]\!] \mathbf{b}_{KI} \tag{50}$$

The normal part δ_{n}, i.e. the crack opening and the tangential part δ_{t}, the crack sliding is given by

$$\delta_{\mathrm{n}} = [\![\mathbf{u}(\mathbf{X})]\!]_n = \mathbf{n} \cdot [\![\mathbf{u}(\mathbf{X})]\!] \tag{51}$$
$$\delta_{\mathrm{t}} = [\![\mathbf{u}(\mathbf{X})]\!]_\tau = \|[\![\mathbf{u}(\mathbf{X})]\!] - (\delta_{\mathrm{n}}\mathbf{n})\| \tag{52}$$

More details are given in Belytschko et al. [6]. If not mentioned otherwise, we only consider normal forces and neglect mode II effects.
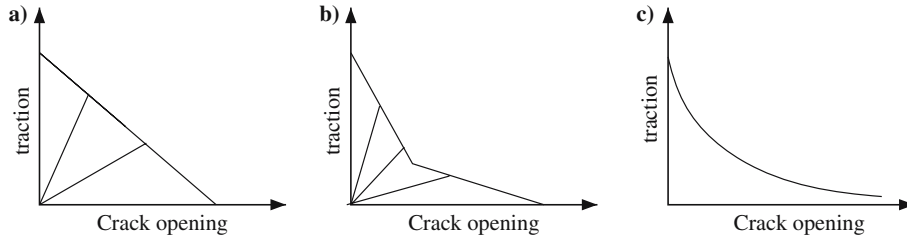
Fig. 6 Cohesive models: **a** linear models, **b** bilinear models, **c** exponential models
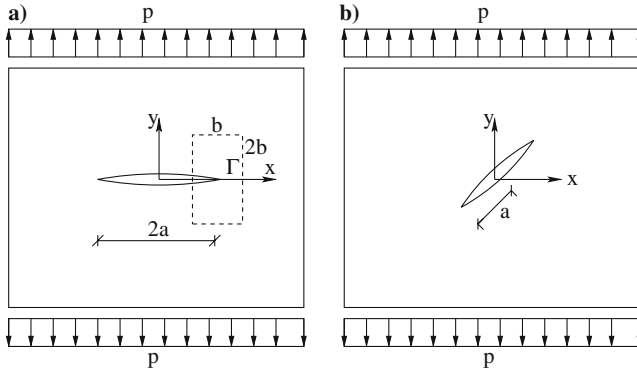

Fig. 7 a Mode I problem, **b** (mixed) mode I–II problem

Fig. 8 The Griffith problem

6.2.3 Cohesive law

The cohesive laws that are most popularly used are shown in Fig. 6. We used linear and exponentially decaying cohesive laws among them because of their simplicity.

7 Verification using linear elastic fracture mechanics

7.1 Crack problem

Consider a mode I crack problem illustrated in Fig. 7a. Plane strain conditions and linear elastic material behaviour are assumed. For an infinite plate, Westergaard [42] provided a solution for this problem:

$$
\sigma_{xx} = p \left(\frac{r_0}{\sqrt{r_1\, r_2}} \cos\left(\phi_0 - \frac{\phi_1 + \phi_2}{2}\right) \right.
$$
$$
\left. - \frac{a^2\, r_0}{(r_1\, r_2)^{1.5}} \sin\phi_0 \sin\left[1.5\,(\phi_1 + \phi_2)\right] - 1 \right)
\tag{53}
$$

$$
\sigma_{yy} = p \left(\frac{r_0}{\sqrt{r_1\, r_2}} \cos\left(\phi_0 - \frac{\phi_1 + \phi_2}{2}\right) \right.
$$
$$
\left. + \frac{a^2\, r_0}{(r_1\, r_2)^{1.5}} \sin\phi_0 \sin\left[1.5\,(\phi_1 + \phi_2)\right] \right)
\tag{54}
$$

$$
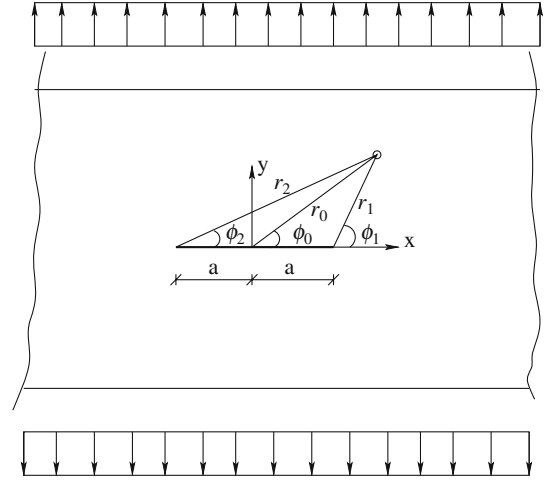\tau_{xy} = p \frac{a^2\, r_0}{(r_1\, r_2)^{1.5}} \sin\phi_0 \cos\left[1.5(\phi_1 + \phi_2)\right]
\tag{55}
$$

where the parameters $r_0, r_1, r_2, \phi_0, \phi_1$ and ϕ_2 are explained in Fig. 8. The exact tractions may be calculated from Eqs. (53) to (55) and are applied to the boundary shown in Fig. 7. The near tip stress field is given by

$$
\sigma_{xx}(r, \phi) = \frac{K_{\mathrm{I}}}{\sqrt{2\pi r}} \cos\frac{\phi}{2} \left(1 - \sin\frac{\phi}{2} \sin\frac{3\phi}{2}\right)
\tag{56}
$$

$$
\sigma_{yy}(r, \phi) = \frac{K_{\mathrm{I}}}{\sqrt{2\pi r}} \cos\frac{\phi}{2} \left(1 + \sin\frac{\phi}{2} \sin\frac{3\phi}{2}\right)
\tag{57}
$$

$$
\tau_{xy}(r, \phi) = \frac{K_{I}}{\sqrt{2\pi r}} \sin\frac{\phi}{2} \cos\frac{\phi}{2} \cos\frac{3\phi}{2}
\tag{58}
$$

with polar coordinates r and ϕ. The stress intensity factor for the Griffith problem is dependent on the boundary condition and the loading type, and for the quasi-static problem in Fig. 7, is given by $K_{\mathrm{I}} = p\sqrt{\pi a}$ where p is the external traction. In numerical simulations, the relation between the J-integral and K_{I} is used to check the local convergence near the crack tip;

$$
J = K_{\mathrm{I}}^2 \frac{1 - \nu^2}{E}
\tag{59}
$$

The J-integral gives the change in strain energy with a unit change in the crack length a and may be calculated by

$$
J = \int_{\Gamma} \left(w\, \mathrm{d}y - \mathbf{t}\frac{\partial \mathbf{u}}{\partial x}\mathrm{d}\Gamma \right)
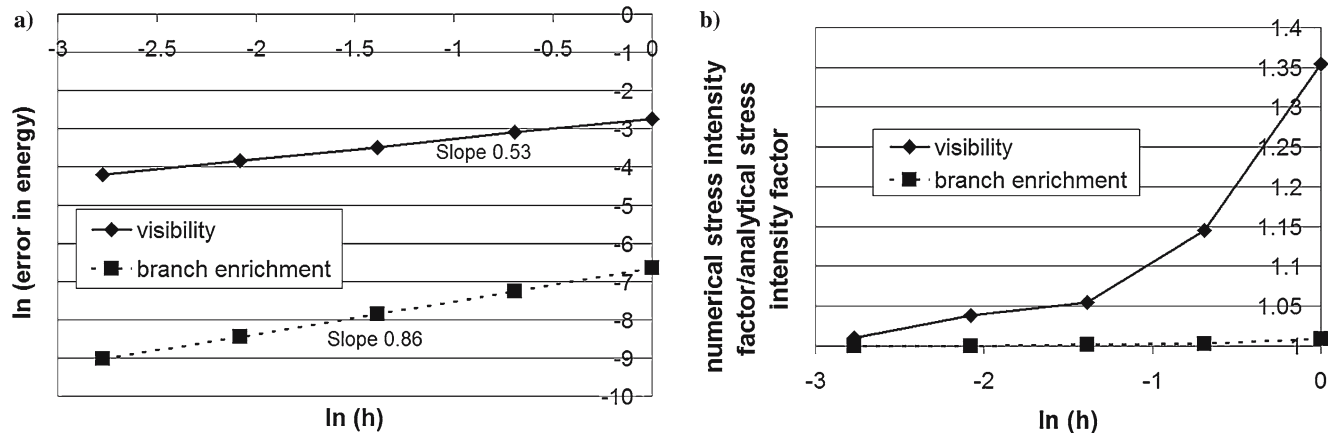\tag{60}
$$

a)

b)

Fig. 9 a Error in the energy for the *mode I* problem; **b** normalized stress intensity factor versus h

where $w = \int_0^\epsilon \sigma : d\epsilon$ is the energy density, $\mathbf{t}$ the traction, $\mathbf{u}$ the displacements and Γ the path around the crack tip as illustrated in Fig. 7. The integration path Γ is chosen to completely encompass the enriched region near the crack tip.

We will study the error in the energy given by

$$\|\text{err}\|_{\text{energy}} = \frac{\|\mathbf{u}_h - \mathbf{u}_{\text{analytic}}\|_{\text{energy}}}{\|\mathbf{u}_{\text{analytic}}\|_{\text{energy}}} \qquad (61)$$

with

$$\|\mathbf{u}\|_{\text{energy}} = \left(\int_{\Omega_0} \mathbf{E}^{\mathrm{T}}(\mathbf{u}) : \mathbf{C} : \mathbf{E}(\mathbf{u}) \, d\Omega_0 \right)^{1/2} \qquad (62)$$

where $\mathbf{E}$ is the Green strain. Additionally, we will check stress intensity factors K_{I} to compare local convergence. Note the branch enrichment in Eq. (5) is used for the linear elasticity problems.

The error in the energy norm is illustrated in Fig. 9a for the mode I problem. We have also included results obtained by EFG with visibility criterion. The local partition of unity enrichment gives more accurate results and a better convergence rate than the crack approach with visibility criterion. This is expected due to the crack tip enrichment with the Westergaard solution. Also local convergence is obtained much faster by the local partition of unity enrichment as shown in Fig. 9b.

7.2 The mode I–II problem

Let us consider a (mixed) mode I–II problem. We study again the error in the energy norm. The analytical near-tip field solution for this problem is given e.g. by Saehn [38]:

$$\sigma_r = \frac{1}{4\sqrt{2\pi r}} \left[K_{\mathrm{I}} \left(5 \cos \frac{\theta}{2} - \cos \frac{3\theta}{2} \right) \right.$$
$$\left. + K_{\mathrm{II}} \left(-5 \sin \frac{\theta}{2} + 3 \sin \frac{3\theta}{2} \right) \right] \qquad (63)$$

$$\sigma_\theta = \frac{1}{4\sqrt{2\pi r}} \left[K_{\mathrm{I}} \left(3 \cos \frac{\theta}{2} - \cos \frac{3\theta}{2} \right) \right.$$
$$\left. + K_{\mathrm{II}} \left(-5 \sin \frac{\theta}{2} + 3 \sin \frac{3\theta}{2} \right) \right] \qquad (64)$$

$$\tau_{r\theta} = \frac{1}{4\sqrt{2\pi r}} \left[K_{\mathrm{I}} \left(\sin \frac{\theta}{2} + \sin \frac{3\theta}{2} \right) \right.$$
$$\left. + K_{\mathrm{II}} \left(\cos \frac{\theta}{2} + \cos \frac{3\theta}{2} \right) \right] \qquad (65)$$

where r and θ are explained in Fig. 10 and with $K_{\mathrm{I}} = \sigma_n \sqrt{\pi a}$ and $K_{\mathrm{II}} = \tau_n \sqrt{\pi a}$, with the loading conditions σ_n and τ_n from Fig. 10 and where

$$\sigma_{ny} = \frac{\sigma_{\bar{x}} + \sigma_{\bar{y}}}{2} + \frac{\sigma_{\bar{x}} - \sigma_{\bar{y}}}{2} \cos 2\alpha \qquad (66)$$

$$\sigma_{nx} = \frac{\sigma_{\bar{x}} + \sigma_{\bar{y}}}{2} - \frac{\sigma_{\bar{x}} - \sigma_{\bar{y}}}{2} \cos 2\alpha \qquad (67)$$

$$\tau_{nxy} = \frac{\sigma_{\bar{x}} - \sigma_{\bar{y}}}{2} \sin 2\alpha \qquad (68)$$

We study again the error in the energy norm and compare it to the error obtained by the visibility method. The same tendency as for the mode I crack is observed for the mixed mode problems (see Fig. 10). Again, the local partition of unity enrichment gives more accurate results and a higher convergence rate. However, the error is larger than the one in the previous example (Fig. 11).

8 Examples

In the following sections, we will present results for several quasi-static and dynamic problems, in which the traction on the crack surface is given by the cohesive crack model. Therefore, the branch enrichment in Eq. (6) is used. Prenotches are assumed to be traction-free. We show the results with $m = 1$ in Eq. (6), since the enrichment with higher m gave very similar results. In all our examples, we used a structured uniform particle arrangement if not stated otherwise. This appears at
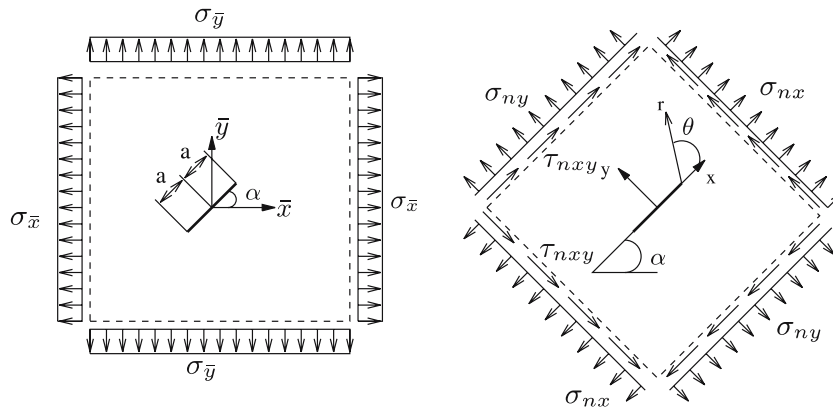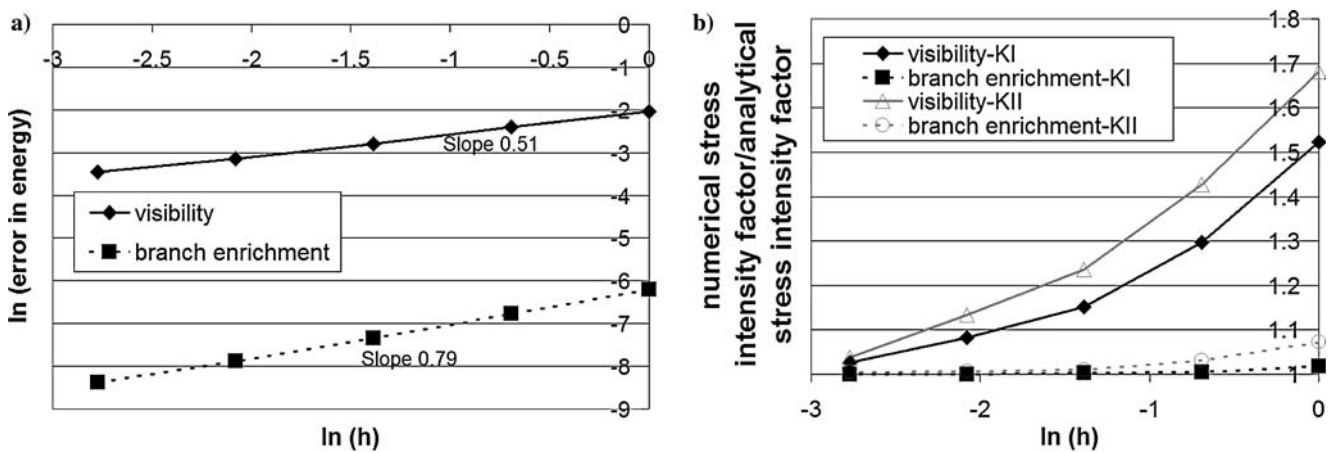
Fig. 10 Mixed mode crack problem

Fig. 11 a Error in the energy for the mode I problem; **b** normalized stress intensity factor versus h

first to be dissonant with the philosophy of meshfree methods. However, a structured particle arrangement is advantageous when incorporating features such as adaptivity. It also facilitates pre- and postprocessing.

8.1 Quasi-static examples

8.1.1 Arrea–Ingraffea beam

The first example is the Arrea and Ingraffea [4] beam. The beam is loaded at two points as shown in Fig. 12. The initial elastic modulus is 28,000 MPa, tensile strength is 2.8 MPa, Poisson's ratio $\nu = 0.18$ and the fracture energy is $G_f = 100$ N/m. The beam failed due to a mixed tensile/shear failure. We have used the Lemaitre [28] model for the continuum in tension and the loss of hyperbolicity condition for the crack initiation and growth. A linear decaying cohesive law is used. The critical crack opening displacement δ_c beyond which the cohesive traction is reduced to zero is calculated as $\delta_c = 2G_f/f_t$ in which f_t is the traction at which the material at the crack tip loses its hyperbolicity. The concrete is
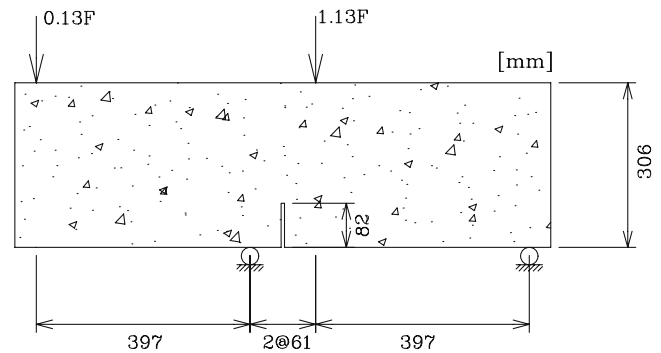

Fig. 12 The tensile/shear beam from Arrea–Ingraffea

assumed to be linear elastic in compression. The beam is discretized with approximately 2,000 and 7,800 particles.

The crack path for the fine particle distribution is shown in Fig. 13. The curvature of the crack is similar to the one in the experiment. The load-displacement curves (measured at the right of the notch) are shown in Fig. 14 and lie in the experimental scatter. We note that we need significantly less particles to obtain convergent results in the load–deflection
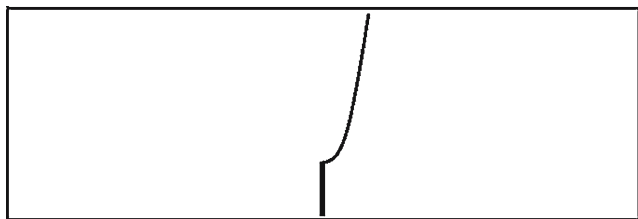
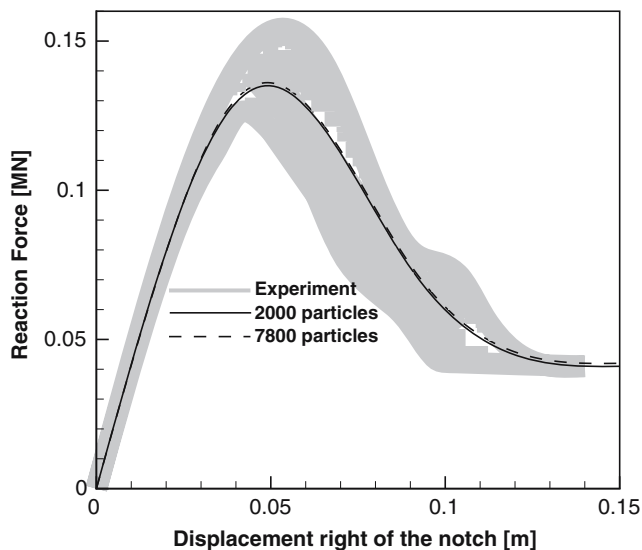**Fig. 13** Crack pattern of the Arrea–Ingraffea beam

Fig. 14 Load–deflection curve of the tensile/shear beam from Arrea–Ingraffea for different numbers of particles

Fig. 15 The four-point-bending beam with two notches from Bocca et al. [15]

Fig. 16 Load–deflection curve of the four-point-bending beam with two notches from Bocca et al. [15]

curve than the 'cracking particle' method described in Rabczuk and Belytschko [34], where approximately 13,000 particles were necessary.

We tested also the influence of higher order branch functions. Though higher order branch functions provide a better stress distribution around the crack tip, the influence with regard to the overall crack pattern or the load–deflection curve is not very high.

8.1.2 Four-point-bending with two notches

Consider a four-point beam in bending with two notches as shown in Fig. 15. Experimental data were given by Bocca et al. [16]. The Lemaitre [28] material model and the loss of hyperbolicity for the crack initiaion and growth, and a linear decaying cohesive law are employed. The material parameters are: $E = 27,000\,\mathrm{MPa}$, $v = 0.18$, $f_\mathrm{t} = 2.0\,\mathrm{MPa}$, $G_\mathrm{f} = 100\,\mathrm{N/m}$ where E is Young's modulus, v is Poisson ratio, f_t the tensile strength and G_f the fracture energy. Number of particles between 660 and 160,000 are studied.

The load–deflection curve is shown in Fig. 16 and agrees very well with the experiment. At 2,550 particles, mesh dependence is completely removed. However, the load–deflection curve even with 660 particles was very close to the converged
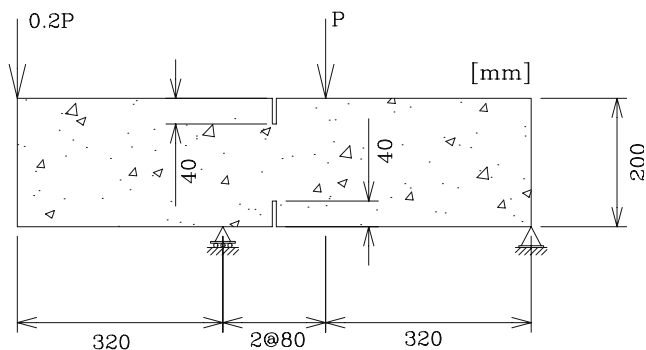
one. The final crack patterns for computations with different numbers of particles are illustrated in Fig. 18. The crack path is obtained by storing the coordinates of the crack tip.

The crack patterns agree very well with the experimental crack pattern. Again, we need only a few particles to obtain good results. With the 'cracking particle' method in [34], 4,000 particles did neither give an appropriate crack path nor a reasonable load–deflection curve. At a number of 2,550 particles, we get here mesh independent results in the load–deflection curve and the crack path.

In Fig. 17, the enriched particles are shown. The enriched nodes for the 660 particle discretization is shown in Fig. 17a. The enriched region of one crack is overlapped with that of the other. This results in a steeper crack path. This problem can be overcome by decreasing the support size slightly, see Fig. 18a. Usually, the support size is chosen to be 3.5 times the particle separation. By decreasing this support size so that
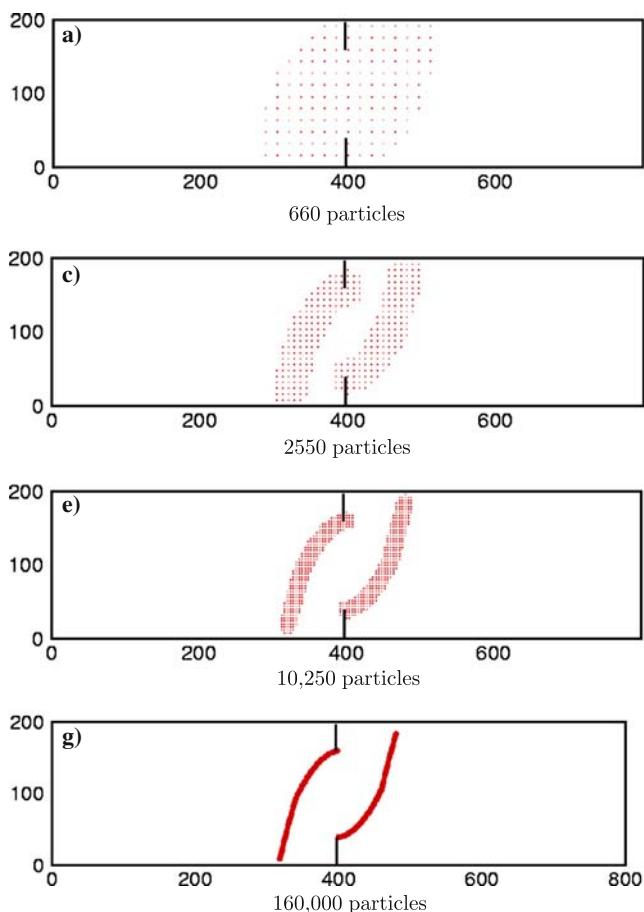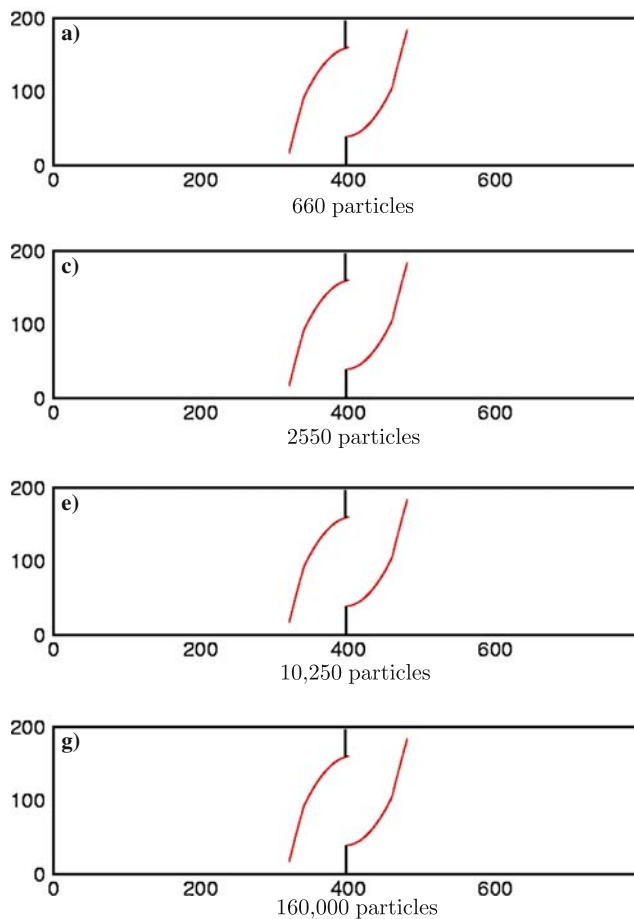
Fig. 17 Enriched nodes of the two notched beam

Fig. 18 Crack paths of the two notched beam

the cracked particles of one crack are not influenced by the other crack, improves the crack paths.

8.2 Dynamic examples

8.2.1 Kalthoff problem

Kalthoff and Winkler [25] performed a series of experiments in which a steel plate was hit by a projectile with different impact velocities as shown in Fig. 19. They discovered different failure phenomena for different impact velocities. Up to a certain velocity of the projectile $v_c = 20$ m/s, the steel plate fails brittle and a crack develops in a 70° angle against the axis parallel to the flight direction of the projectile. When the velocity exceeds v_c, they found a completely different failure pattern. A shear band develops from the onset of the notch in a much flatter angle of the opposite direction. We will first focus on the brittle failure pattern and an impact velocity of 17 m/s.

We used 1,700, 6,500 and 26,000 particles in our simulations. We tested two material models, the Johnson–Cook model [24] and the Lemaitre [28] model. The latter model was applied in Belytschko et al. [6] for the Kalthoff problem and a brittle failure mechanism. For the Lemaitre model, the
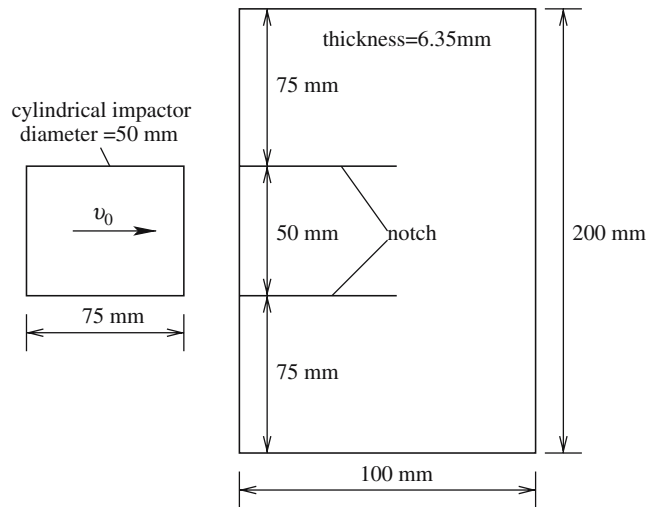

Fig. 19 The Kalthoff problem: test setup

material parameters are: Young's modulus $E = 190$ GPa, Poisson ratio $\nu = 0.3$, fracture energy $G_f = 22,170$ J/m^2, critical crack opening displacement $\delta_{max} = 5.378 \times 10^{-5}$ m, damage threshold $\epsilon_{D_0} = 3 \times 10^{-3}$ and parameters $A = 1.0$
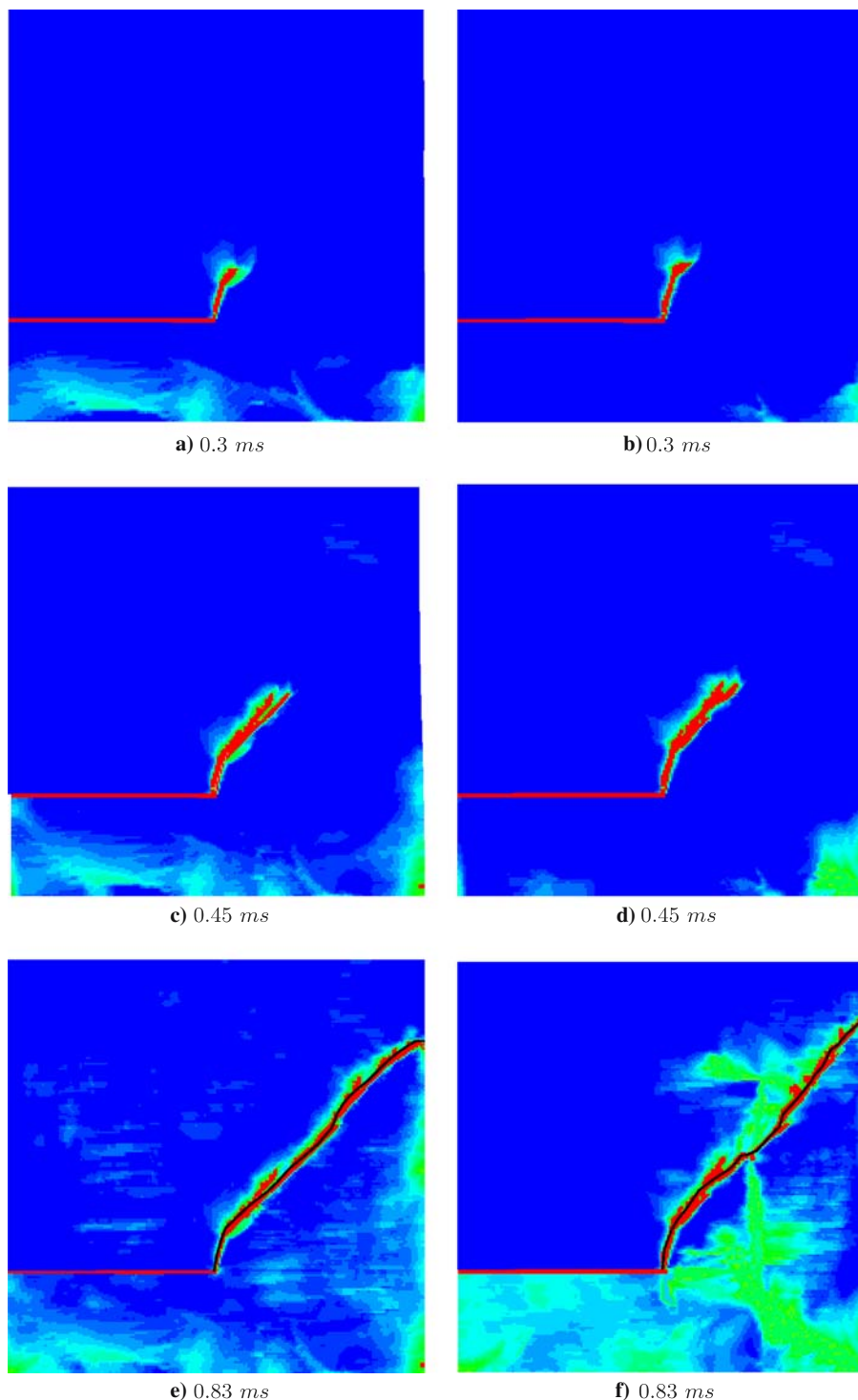
a) $0.3\ ms$

b) $0.3\ ms$

c) $0.45\ ms$

d) $0.45\ ms$

e) $0.83\ ms$

f) $0.83\ ms$

Fig. 20 a, c, e Crack pattern for the 26,000 particle arrangement, **b, d, f** crack pattern for the 1,700 particle arrangement using the new approach

and $B = 200$. The material parameters of the Johnson–Cook model are: $A = 2\,\text{GPa}$, $B = 94.5\,\text{GPa}$, $C = 0.0165$, $T_0 = 293\,\text{K}$, $\gamma_0 = 1.3 \times 10^{-13}\,\text{s}^{-1}$ and $\kappa_0 = 500\,\text{K}$. An exponential cohesive law is used.

We exploited the symmetry in our discretization. The crack paths for the Lemaitre model is shown in Fig. 20 for two different numbers of particles. The experimental crack angle at the prenotch of $70°$ versus the crack orientation is reproduced well by our simulation. However, in the course of the computation, the crack starts to curve and gets flatter. A similar crack pattern was obtained by Xu and Needleman [43]. The damage is plotted in Fig. 20. A higher damage at
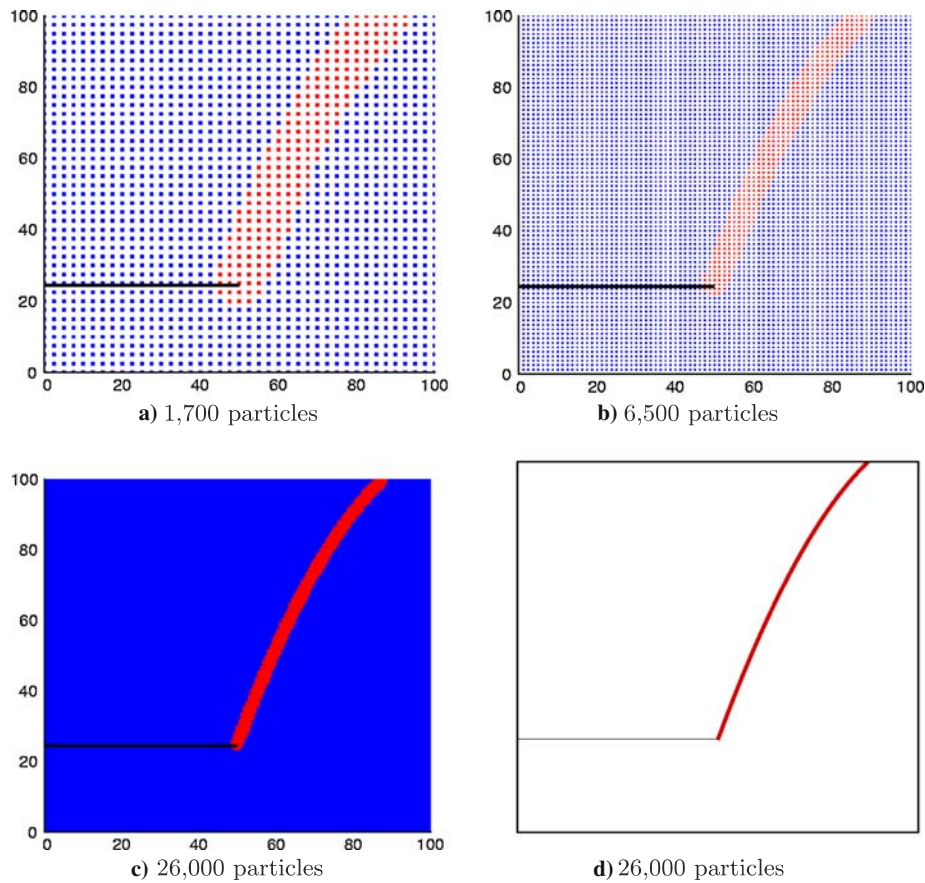
a) 1,700 particles

b) 6,500 particles

c) 26,000 particles

d) 26,000 particles

Fig. 21 Kalthoff problem with brittle failure for different particle refinements; **a–c** Enriched nodes (*red colour*); **d** crack pattern

the right lower corner occurs in Fig. 20b, d, f. However, no crack initiates. The crack is shown as solid line at the end of the computation. We therefore conclude that the Lemaitre model is not well suited to model crack propagation for the Kalthoff problem.

The results of the different particle arrangement for the Johnson Cook model are shown in Fig. 21. As in Fig. 20, only the upper part of the specimen is illustrated. Particles enriched are shown in red colour.

The crack is shown in Fig. 21d for the 26,000 particle discretization and is almost identical with the crack pattern of the coarser simulations. The experimental crack angle at the prenotch of 70° versus the crack orientation is reproduced well by our simulation. The crack path is very smooth.

Figure 22 shows the speed of the crack tip for the three different refinements. The Rayleigh wave speed is never exceeded and the course of the crack speed looks very similar. For the coarsest discretization with 1,700 particles, the crack starts to propagate a little later. The course of the crack speed is similar to the one obtained in Belytschko et al. [6].

We increased the impact velocity to 30 m/s, at which a ductile failure appeared in the experiments. The failure pattern of our simulation is shown in Fig. 23; enriched nodes are plotted in red colour. We were able to reproduce the failure mode of the experiment well. Only 1,700 particles are needed to resolve the shear band. The results do not show any mesh
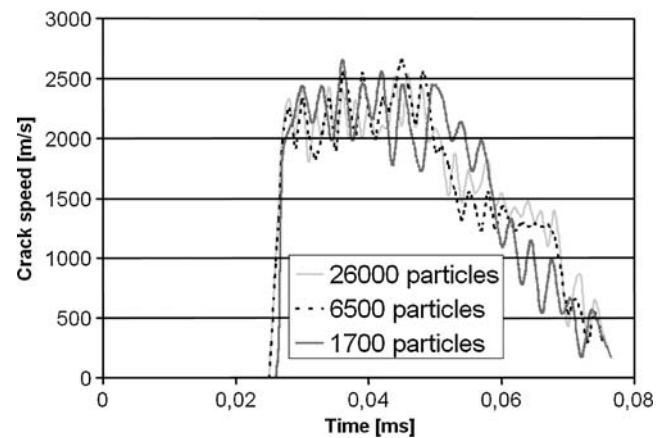

Fig. 22 Crack speed time history of the Kalthoff problem with brittle failure

dependence. Note, that for the shear band we allow only tangential jumps in the displacement field while normal jumps are suppressed. For details of this concept, see Belytschko et al. [13].

8.2.2 Crack branching

In the following, we examine the performance of the method in a crack branching problem. Consider a rectangular
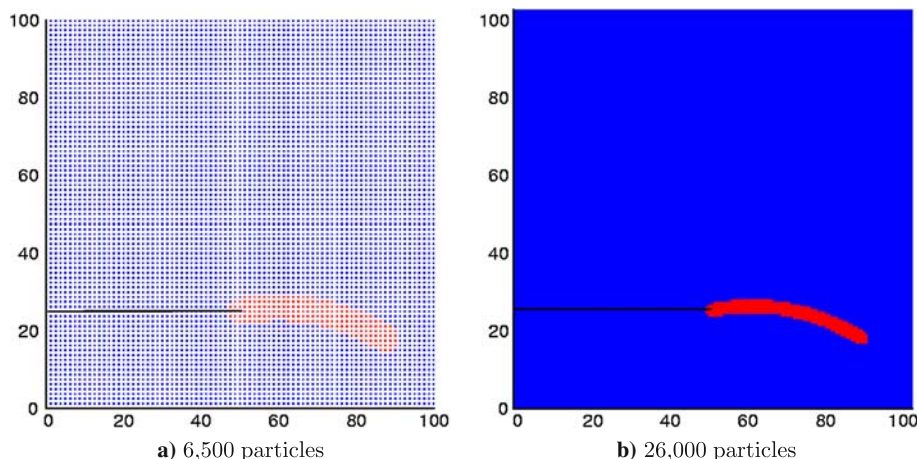
a) 6,500 particles   **b)** 26,000 particles

Fig. 23 a, b Kalthoff problem with ductile failure for different particle refinements; enriched nodes are plotted in *red colour*

prenotched specimen as shown in Fig. 24. The length of the rectangle is 0.1 m and width 0.04 m. Initially, a horizontal crack is placed from the left edge to the center of the plate. Tensile tractions of 1 MPa are applied on the top and bottom edges.

We used the Lemaitre [28] damage law, loss of hyperbolicity and we tested different cohesive laws. We will present the results for an exponential decaying law. The material constants are $\varrho = 2,450 \,\text{kg/m}^3$, $E = 32 \,\text{MPa}$, $\nu = 0.2$ and $A = 1.0$, $B = 7,300$ and $\epsilon_{D_0} = 8.5 \times 10^{-5}$ for the Lemaitre model. Computations of this problem have previously been reported by Xu and Needleman [43], Falk et al. [20], Belytschko et al. [6] and Rabczuk and Belytschko [34]. Experimental data is available, too; see Ravi-Chandar [36], [40] or [21], but for different dimensions.

We used discretizations with approximately 4,000–16,000 particles. In contrast to Rabczuk and Belytschko [34], we applied the load as ramp, meaning the maximum load of 1 MPa is reached linearly within 0.001 ms. An abrupt loading led to difficulties in tracing the crack paths. The crack pattern is shown in Fig. 25 for different particle refinements and does not show mesh dependence. Note that we added for illustration purposes additional interpolation points for the coarse discretization. The crack started to branch at approximately 0.03 ms. No more branching occurred in the course of the simulation. Our crack pattern looks similar to the one obtained in Belytschko et al. [6].

As in [6], we suffer some difficulties in advancing the crack paths. One of the most difficult tasks is to decide if the crack branches or not. This depends on the radius of the circle around the crack tip where loss of hyperbolicity is checked.

As already noticed in Belytschko et al. [6], in dynamics, the cracktip direction and speed can become rather erratic. Therefore, they smoothed the direction by using an average of the current and several preceding directions. We will use another approach and smooth the stresses around the crack tip with a smooth meshfree shape function. One might question if this is necessary in meshfree methods but we found out that the branching enrichment causes some numerical noise. We used dynamic damping, i.e. added a damping term $\alpha \mathbf{v}$ in
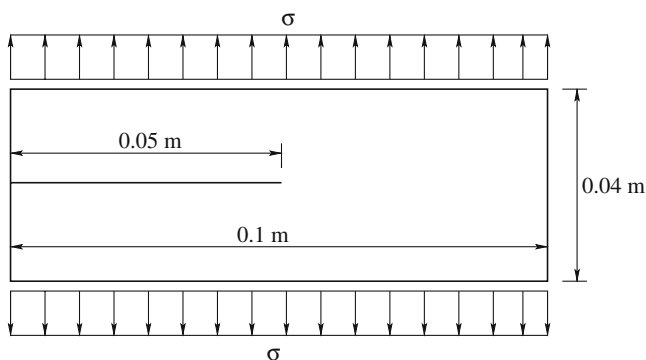

Fig. 24 Plate with an edge crack

the equation of motion, where α is a damping parameter that should be chosen small since it may influence wave effects and $\mathbf{v}$ is the particle velocity.

The time history of the crack speed is shown in Fig. 26. Both discretizations give a similar course of the crack speed. The crack starts to propagate at about 0.012 ms. As expected, the crack speed is the highest at the time of crack branching. At that point, the crack speed almost reaches the theoretical Rayleigh wave speed. Afterwards, the crack branches and the crack speed decreases. The crack speed of only the upper branch is shown in the figure. The crack speed of the lower branch is very similar as Fig. 25 might indicate.

We tested higher order branch functions. The results in the crack pattern were marginal.

8.3 Multiple cracking with crack junctions

Our last example is multiple cracking with crack junctions. Therefore, consider a square cell with several precracks. It is assumed that the precracks are traction-free. This problem was studied by the cracking particle method to investigate microcracking of a unit cell under uniaxial and biaxial tension. We will study two unit cells with five precracks of different sizes as shown in Fig. 27a, b in this paper.
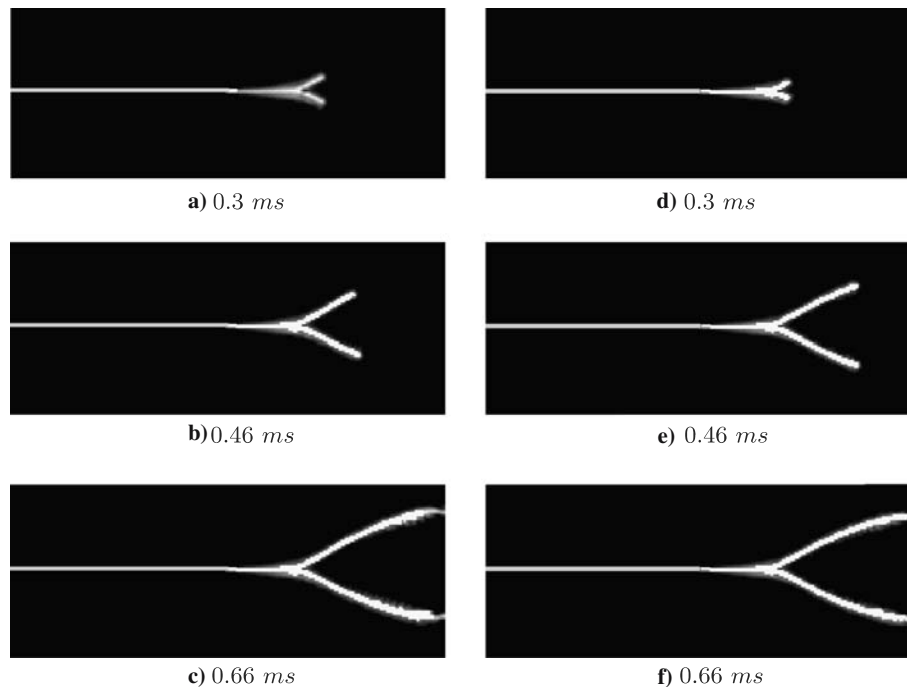
a) $0.3 \; ms$

d) $0.3 \; ms$

b) $0.46 \; ms$

e) $0.46 \; ms$

c) $0.66 \; ms$

f) $0.66 \; ms$

Fig. 25 Crack pattern of the prenotched specimen at different t time steps for **a–c** 4,000 particles, **d–f** 16,000 particles; for a better illustration, additional interpolation points are added in the **a–c**
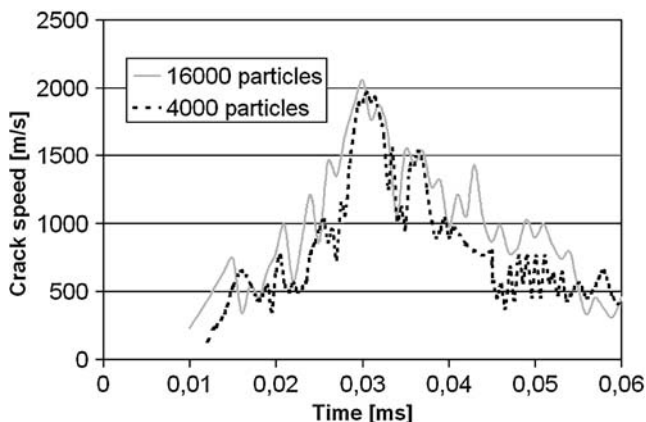

Fig. 26 Crack speed time history for the crack branching problem

The unit cell is discretized with two different refinements, 1,600 and 6,400 particles. The Lemaitre [28] damage model is used in tension and linear elastic behaviour is assumed in compression. We will compare the results to those obtained with the cracking particle method in which approximately 23,000 particles were used. The crack pattern at an intermediate step and the final crack pattern for the cracking particle method is shown in Figs. 27a–f. In Figs. 27d–f we considered longer precracks. The final crack pattern of our new approach is shown in Figs. 27g,h. The results are mesh-independent and very similar to the ones obtained with the cracking particle method. However, we need significantly less particles compared to the cracking particle method. An experimental result is shown in Fig. 27i.

The crack patterns for different precrack sizes are different. For small precracks, cracks propagate from the onset of the precrack perpendicular to the load direction. In the lower part of the unit cell where two preflaws are located, the cracks join in the middle of the specimen. The same tendency is observed for longer precracks. However, in the upper part where three precracks are located, the cracks subdivide the specimen into four parts when the precracks are sufficiently small while for larger precracks, three fragments occur. This is due to the fact that for the latter case, the two upper cracks join and hence unload the region below. The cracks in the lower region are arrested. If the cracks are small, the middle precrack joins with the upper right precrack.

9 Conclusion

We have presented a meshfree method – extended element free Galerkin method (XEFG) – for crack propagation problems. The method is based on the introduction of a discontinuity in the displacement field after the material looses stability. The crack tip enrichment with branch functions is employed. A cohesive model is used that solely depends on the discontinuous part of the displacement field.

The method is applied to several static and dynamic problems where experimental or other numerical data is available. It is also applied to mode I and I-II crack problems of which the analytical solutions are available. The method is very accurate. It resolves the crack path with low particle resolutions. In two dimensions, more than 10 times less particles were necessary than in the *cracking particle* method, [34].
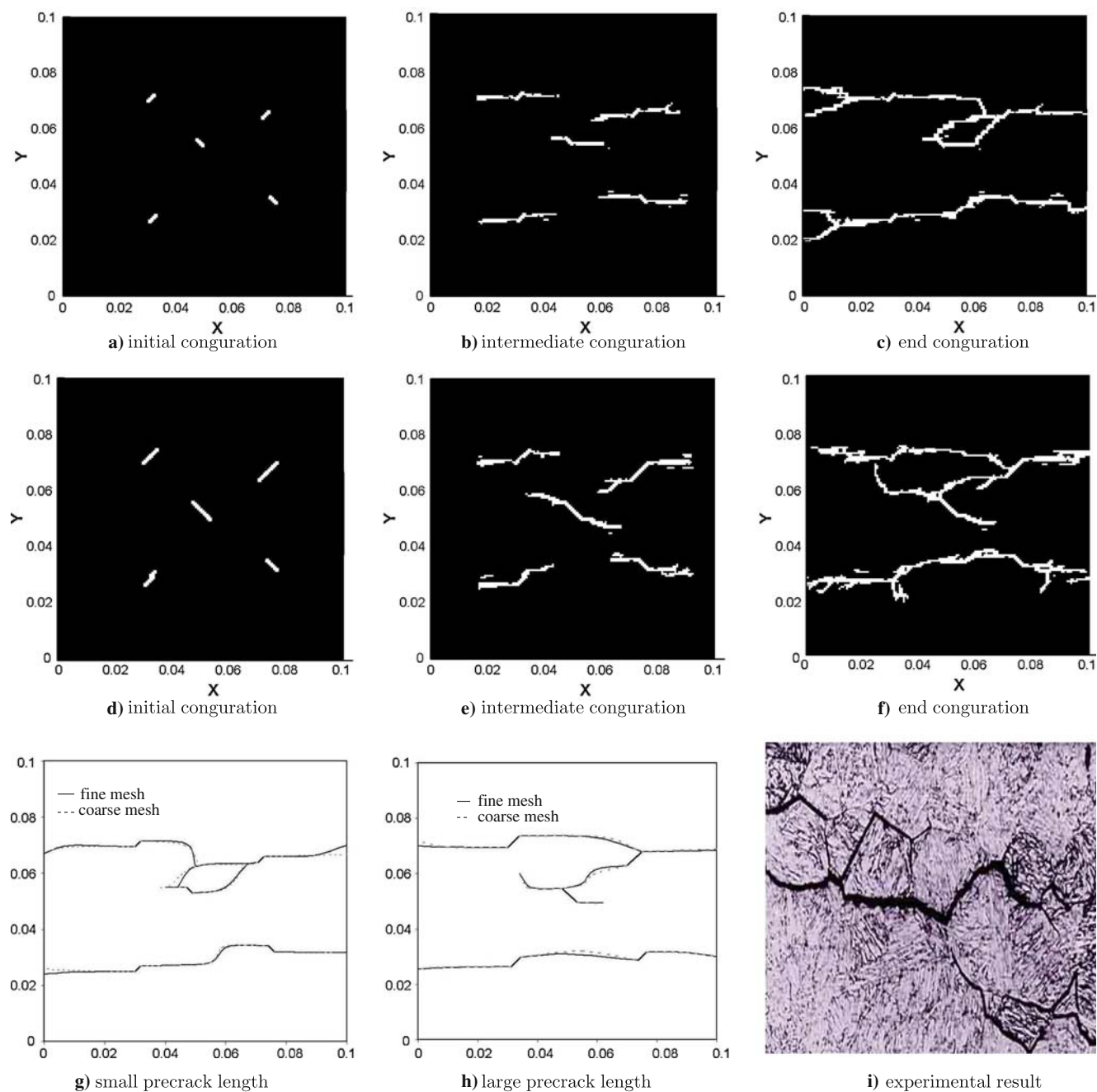
Fig. 27 Crack pattern of the precracked unit cell at different load steps and for different precrack sizes, **a–f** cracking particle method, **g–h** new approach, **i** experimental microcrack-result

We tested different branch enrichments. Higher order branch function did not improve the overall-results significantly in the examples that we tested. The overall crack pattern was almost the same. However, higher order branch functions give a better stress distribution around the crack tip.

Most difficulties arise in dynamic crack propagation problems. Some *smoothing* of the crack paths, e.g. from the direction of the previous step or by a stress projection method, is still needed. Otherwise, the crack paths would have rather a zig-zag shape. This problem, even for statics, was reported by other authors, e.g. Belytschko et al. [6]; Areias and Belytschko [1], and can be attenuated by above mentioned techniques.

It is also not easy to detect branching, especially in cases with high load amplitude and load velocity. We checked loss of material stability within a certain radius around the crack tip. It is sometimes still difficult to determine if an existing crack branches or if there might be a new crack initiation. This is a subject of ongoing investigations.

References

1. Areias PMA, Belytschko T (2005) Analysis of three-dimensional crack initiation and propagation using the extended finite element method. Comput Mech
2. Areias PMA, Song JH, Belytschko T (2006) Analysis of fracture in thin shells by overlapping paired elements (in press)
3. Armero F, Garikipati K (1996) An analysis of strong discontinuities in multiplicative finite strain plasticity and their relation with the numerical simulation of strain localization in solids. Int J Solids Struct 33(20–22):2863–2885
4. Arrea M, Ingraffea AR (1982) Mixed-mode crack propagation in mortar and concrete. Technical Report 81-13, Department of Structural Engineering, Cornell University Ithaka
5. Belytschko T, Black T (1999) Elastic crack growth in finite elements with minimal remeshing. Int J Numer Methods Eng 45(5):601–620
6. Belytschko T, Chen H, Xu J, Zi G (2003) Dynamic crack propagation based on loss of hyperbolicity and a new discontinuous enrichment. Int J Numer Methods Eng 58(12):1873–1905
7. Belytschko T, Fish J, Englemann B (1988) A finite element method with embedded localization zones. Comput Methods Appl Mech Eng 70:59–89
8. Belytschko T, Krongauz Y, Organ D, Fleming M, Krysl P (1996) Meshless methods: An overview and recent developments. Comput Methods Appl Mech Eng 139:3–47
9. Belytschko T, Lu YY (1995) Element-free galerkin methods for static and dynamic fracture. Int J Solids Struct 32:2547–2570
10. Belytschko T, Lu YY, Gu L (1994) Element-free galerkin methods. Int J Numer Methods Eng 37:229–256
11. Belytschko T, Lu YY, Gu L (1995) Crack propagation by element-free galerkin methods. Eng Fracture Mech 51(2):295–315
12. Belytschko T, Moes N, Usui S, Parimi C (2001) Arbitrary discontinuities in finite elements. Int J Numer Methods Eng 50(4):993–1013
13. Belytschko T, Rabczuk T, Samaniego E, Areias PMA (2006) Two- and three dimensional modelling of shear bands using a meshfree method with cohesive surfaces. Int J Numer Methods Eng (in press)
14. Belytschko T, Tabbara M (1996) Dynamic fracture using element-free galerkin methods. Int J Numer Methods Eng 39(6):923–938
15. Bocca P, Carpinteri A, Valente S (1991) Mixed model fracture of concrete. Int J Solids Struct 33:2899–2938
16. Bocca P, Carpintieri A, Valente S (1990) Size effect in the mixed mode crack propagation: softening and snap-back analysis. Eng Fracture Mech 35:159–170
17. Camacho GT, Ortiz M (1996) Computational modeling of impact damage in brittle materials. Int J Solids and Struct 33:2899–2938
18. Chessa J, Wang H, Belytschko T (2003) On the construction of blending elements for local partition of unity enriched finite elements. Int J Numer Methods Eng 57(7):1015–1038
19. Daux C, Moes N, Dolbow J, Sukumar N, Belytschko T (2000) Arbitrary branched and intersection cracks with the extended finite element method. Int J Numer Methods Eng 48:1731–1760
20. Falk ML, Needleman A, Rice JR (2001) A critical evaluation of cohesive zone models of dynamic fracture. J Phys IV 11(PR5):43–50
21. Fineberg J, Sharon E, Cohen G (2003) Crack front waves in dynamic fracture. Int J Fracture 121(1–2):55–69
22. Gravouil A, Moes N, Belytschko T (2002) Non-planar 3D crack growth by the extended finite element method and level sets – part ii: Level set update. Int J Numer Methods Eng 53:2569–2586
23. Gummalla RR (1999) Effect of material and geometric parameters on deformations of a dynamically loaded prenotched plate. Master's Thesis, Virginia Polytechnical Institute and State University
24. Johnson GR, Cook WH (1983) A constitutive model and data for metals subjected to large strains, high strain rates, and high temperatures. In: Proceedings of the 7th international Symposium on Ballistics
25. Kalthoff JF, Winkler S (1987) Failure mode transition at high rates of shear loading. Int Conf Impact Loading Dyn Behav Mater 1:185–195
26. Krysl P, Belytschko T (1999) The element free galerkin method for dynamic propagation of arbitrary 3-D cracks. Int J Numer Methods Eng 44(6):767–800
27. Laborde P, Pommier J, Renard Y, Solau M (2005) Higher-order extended finite element method for cracked domains. Int J Numer Methods Eng 64(3):354–381
28. Lemaitre J (1971) Evaluation of dissipation and damage in metal submitted to dynamic loading. Proceedings ICM 1
29. Lu YY, Belytschko T, Tabbara M (1995) Element-free galerkin method for wave-propagation and dynamic fracture. Comput Methods Appl Mech Eng 126(1–2):131–153
30. Melenk JM, Babuska I (1996) The partition of unity finite element method: Basic theory and applications. Comput Methods Appl Mech Eng 139:289–314
31. Moes N, Dolbow J, Belytschko T (1999) A finite element method for crack growth without remeshing. Int J Numer Methods Eng 46(1):133–150
32. Moes N, Gravouil A, Belytschko T (2002) Non-planar 3-D crack growth by the extended finite element method and level sets, parti: mechanical model. Int J Numer Methods Eng 53(11):2549–2568
33. Ortiz M, Pandolfi A (1999) Finite-deformation irreversible cohesive elements for three-dimensional crack-propagation analysis. Int J Numer Methods Eng 44:1267–1282
34. Rabczuk T, Belytschko T (2004) Cracking particles: a simplified meshfree method for arbitrary evolving cracks. Int J Numer Methods Eng 61(13):2316–2343
35. Rabczuk T, Belytschko T (2005) Adaptivity for structured meshfree particle methods in 2D and 3D. Int J Numer Methods Eng 63(11):1559–1582
36. Ravi-Chandar K (1998) Dynamic fracture of nominally brittle materials. Int J Fracture 90(1–2):83–102
37. Remmers JJC, de Borst R, Needleman A (2003) A cohesive segments method for the simulation of crack growth. Comput Mech 31:69–77
38. Saehn S. Technische Bruchmechanik, Vorlesungsmanuskript. Technische Universitaet Dresden, Institut fuer Festkoerpermechanik
39. Samaniego E, Oliver X, Huespe A (2003) Contributions to the continuum modelling of strong discontinuities in two-dimensional solids. PhD thesis, International Center for Numerical Methods in Engineering, Monograph CIMNE No. 72
40. Sharon E, Fineberg J (1996) Microbranching instability and the dynamic fracture of brittle materials. Phys Rev B 54(10):7128–7139
41. Ventura G, Xu J, Belytschko (2002) A vector level set method and new discontinuity approximations for crack growth by efg. Int J Numer Methods Eng 54(6):923–944
42. Westergaard HM (1939) Bearing pressures and cracks. J Appl Mech 6:A49–A53
43. Xu X-P, Needleman A (1994) Numerical simulations of fast crack growth in brittle solids. J Mech Phys Solids 42:1397–1434
44. Zhou F, Molinari JF (2004) Dynamic crack propagation with cohesive elements: a methodolgy to address mesh dependence. Int J Numer Methods Eng 59(1):1–24
45. Zi G, Belytschko T (2003) New crack-tip elements for xfem and applications to cohesive cracks. Int J Numer Methods Eng 57(15):2221–2240
46. Zi G, Chen H, Xu J, Belytschko T (2005) The extended finite element method for dynamic fractures. Shock Vib 12(1):9–23
47. Zi G, Song J-H, Budyn E, Lee S-H, Belytschko T (2004) A method for grawing multiple cracks without remeshing and its application to fatigue crack growth. Model Simul Materials Sci Eng 12(1):901–915